Article

Cell

Epigenetic Activation of WNT5A Drives Glioblastoma Stem Cell Differentiation and Invasive Growth

Graphical Abstract

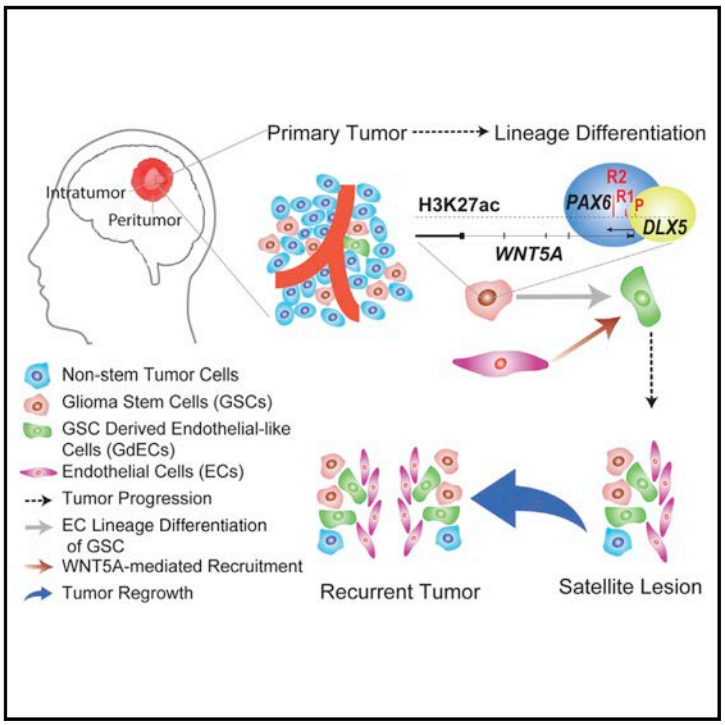

Authors

Baoli Hu, Qianghu Wang, Y. Alan Wang, ..., Lynda Chin, Roeland G.W. Verhaak, Ronald A. DePinho

Correspondence

yalanwang@mdanderson.org (Y.A.W.), rdepinho@mdanderson.org (R.A.D.)

In Brief

Epigenetic activation of WNT5A expression contributes to glioblastoma tumor recurrence by promoting differentiation of glioma-derived stem cells into endothelial cells.

Highlights

- Comparisons of NSCs and derivative GSCs reveal elevated WNT5A and EC signature
- PAX6/DLX5 bidirectionally regulates WNT5A during differentiation of GSCs into GdECs
- WNT5A-mediated GdEC differentiation and EC recruitment support GSC invasive growth
- Clinical studies of peritumoral/recurrent GBM reveal increased WNT5A/GdEC expression

Data Resources

GSE85615
GSE86624

Hu et al., 2016, Cell *167*, 1281–1295
November 17, 2016
http://dx.doi.org/10.1016/j.cell.2016.10.039

CellPress

Article

Cell

Epigenetic Activation of WNT5A Drives Glioblastoma Stem Cell Differentiation and Invasive Growth

Baoli Hu,[1,16] Qianghu Wang,[2,3,16] Y. Alan Wang,[1,16,*] Sujun Hua,[1] Charles-Etienne Gabriel Sauvé,[1] Derrick Ong,[1] Zheng D. Lan,[1] Qing Chang,[3,9] Yan Wing Ho,[1] Marta Moreno Monasterio,[1] Xin Lu,[1] Yi Zhong,[4] Jianhua Zhang,[3,9] Pingna Deng,[1] Zhi Tan,[5] Guocan Wang,[1] Wen-Ting Liao,[1] Lynda J. Corley,[6] Haiyan Yan,[10] Junxia Zhang,[11] Yongping You,[11] Ning Liu,[11] Linbo Cai,[12] Gaetano Finocchiaro,[13] Joanna J. Phillips,[14] Mitchel S. Berger,[15] Denise J. Spring,[1] Jian Hu,[1] Erik P. Sulman,[7,8] Gregory N. Fuller,[6] Lynda Chin,[3] Roeland G.W. Verhaak,[2,3] and Ronald A. DePinho[1,17,*]

[1]Department of Cancer Biology
[2]Department of Bioinformatics and Computational Biology
[3]Department of Genomic Medicine
[4]Department of Epigenetics and Molecular Carcinogenesis
[5]Department of Experimental Therapeutics
[6]Department of Pathology
[7]Department of Radiation Oncology
[8]Department of Translational Molecular Pathology
[9]Institute for Applied Cancer Science
University of Texas MD Anderson Cancer Center, Houston, TX 77030, USA
[10]Department of Medical Oncology, Dana-Farber Cancer Institute, Boston, MA 02215, USA
[11]Department of Neurosurgery, The First Affiliated Hospital of Nanjing Medical University, Nanjing 210029, China
[12]Department of Oncology, Guangdong 999 Brain Hospital, Guangzhou 510510, China
[13]Unit of Molecular Neuro-Oncology, Fondazione IRCCS Istituto Neurologico C. Besta, 20133 Milano, Italy
[14]Departments of Neurological Surgery and Pathology
[15]Neurological Surgery
University of California, San Francisco, San Francisco, CA 94143, USA
[16]Co-first author
[17]Lead Contact
*Correspondence: yalanwang@mdanderson.org (Y.A.W.), rdepinho@mdanderson.org (R.A.D.)
http://dx.doi.org/10.1016/j.cell.2016.10.039

SUMMARY

Glioblastoma stem cells (GSCs) are implicated in tumor neovascularization, invasiveness, and therapeutic resistance. To illuminate mechanisms governing these hallmark features, we developed a de novo glioblastoma multiforme (GBM) model derived from immortalized human neural stem/progenitor cells (hNSCs) to enable precise system-level comparisons of pre-malignant and oncogene-induced malignant states of NSCs. Integrated transcriptomic and epigenomic analyses uncovered a PAX6/DLX5 transcriptional program driving WNT5A-mediated GSC differentiation into endothelial-like cells (GdECs). GdECs recruit existing endothelial cells to promote peritumoral satellite lesions, which serve as a niche supporting the growth of invasive glioma cells away from the primary tumor. Clinical data reveal higher WNT5A and GdECs expression in peritumoral and recurrent GBMs relative to matched intratumoral and primary GBMs, respectively, supporting WNT5A-mediated GSC differentiation and invasive growth in disease recurrence. Thus, the PAX6/DLX5-WNT5A axis governs the diffuse spread of glioma cells throughout the brain parenchyma, contributing to the lethality of GBM.

INTRODUCTION

Glioblastoma multiforme (GBM) is a highly lethal primary brain tumor characterized by robust neovascularization and glioma cell invasiveness throughout the brain parenchyma (Dunn et al., 2012; Furnari et al., 2007). Poor prognosis relates to the near universal recurrence of tumors despite aggressive multimodality treatment of maximal surgical resection, radiotherapy, and chemotherapy (Wen and Kesari, 2008). Gliomagenesis is driven by genetic alterations, including those targeting components of the TP53-ARF-MDM2 and PTEN-PI3K-AKT pathways (Cancer Genome Atlas Research Network, 2008; Brennan et al., 2013; Ceccarelli et al., 2016) and can arise from the transformation of neural stem/progenitor cells (NSCs) (Alcantara Llaguno et al., 2009; Zheng et al., 2008).

GBM possesses so-called glioblastoma stem cells (GSCs), which share many NSC features such as expression of stem cell markers (e.g., Nestin, CD133), self-renewal, and multi-lineage differentiation capacity (Furnari et al., 2007; Lobo et al., 2007; Singh et al., 2004). GSCs are associated with strong tumor initiation potential and are thought to contribute to disease progression, recurrence and therapeutic resistance (Bao et al.,

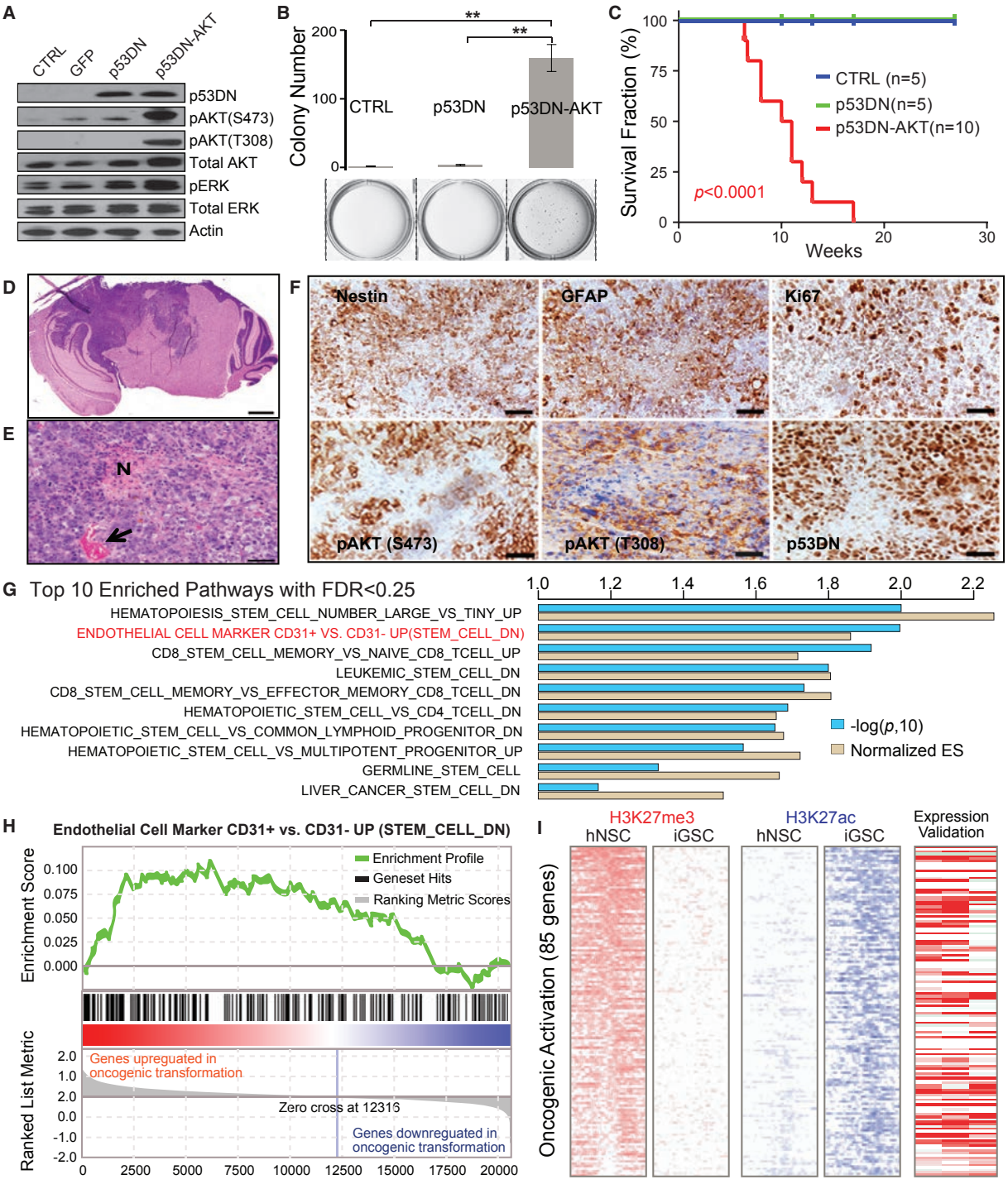

Figure 1. Overexpression of p53DN and myr-AKT Generates Malignant Glioma and Upregulates EC Signaling Pathway

(A) Immunoblot analysis of overexpressed oncogenes in hNSCs.

(B) Soft agar colony formation of hNSCs expressing p53DN, p53DN/myr-AKT (p53DN-AKT). Error bars represent SD of triplicate wells. **p < 0.01. Representative images are shown.

(legend continued on next page)

2006; Chen et al., 2012; Zheng et al., 2008; Zhu et al., 2014). While GSCs exhibit differentiation capacity into glial and neuronal lineages, their terminal differentiation capacity is markedly impaired (Hu et al., 2013; Zheng et al., 2008), and they show trans-differentiation capacity (Cheng et al., 2013; Ricci-Vitiani et al., 2010; Soda et al., 2011; Wang et al., 2010).

The robust developmental plasticity of GSCs has also been evidenced by their capacity to differentiation into endothelial cells (ECs), which display classic EC phenotypes in vitro and have been reported to contribute to GBM vascularization in vivo (Ricci-Vitiani et al., 2010; Wang et al., 2010). The genetic and epigenetic factors driving GSCs differentiation into ECs have not been elucidated; nor is it known how GdECs might contribute to the pathobiology of GBM or to clinical outcomes (Cheng et al., 2013; Rodriguez et al., 2012).

Here, we delineate mechanisms governing the aberrant developmental plasticity of GSCs and its contribution to the refractory nature of GBM. We establish a GBM model that affords a direct comparison of genome-wide histone modifications and associated gene expression alterations between parental human NSCs and their derivative oncogene-induced GSCs (hereafter iGSCs), identifying PAX6- and DLX5-regulated WNT5A as a key factor driving iGSCs differentiation into GdECs. These GdECs function, in turn, to recruit host ECs to form a vascular-like niche that supports the growth of invading glioma cells in the brain parenchyma, a process known to contribute to disease recurrence in the clinic.

RESULTS

EC Signaling Pathway Enrichment in De Novo Gliomagenesis via Oncogenic Transformation of Human NSCs

Consistent with the critical roles of TP53 and PTEN-PI3K-AKT alterations in GBM pathogenesis (Cancer Genome Atlas Research Network, 2008; Brennan et al., 2013), GBM genomic and proteomic profiles from The Cancer Genome Atlas (TCGA) show significant correlation between poorer prognosis and higher levels of AKT activation in patients with TP53 mutations (Figure S1A). These results are consistent with the notion that robust AKT activation promotes disease aggressiveness (Molina et al., 2010; Phillips et al., 2006; Suzuki et al., 2010; Wang et al., 2004).

To model these pathway alterations and establish a de novo human GBM model, we employed Myc-immortalized human NSCs (hNSCs) that were documented to possess NSC-like features including self-renewal, expression of NSC markers, and multi-lineage differentiation capacity (data not shown). The hNSCs were infected with lentiviruses encoding dominant-negative p53 (p53DN) and/or a constitutively active myristoylated form of AKT (myr-AKT) (Figure 1A). The hNSCs transduced with both p53DN and myr-AKT (p53DN-AKT-hNSCs), but not p53DN or myr-AKT alone, exhibited robust soft agar colony formation (Figures 1B and S1B) and highly penetrant tumorigenic potential following intracranial injection in mice (Figure 1C).

Histopathological characterization of the p53DN-AKT-hNSCs derived tumors documented classical GBM features of high cellular density, pseudopalisading necrosis, and microvascular hyperplasia (Figures 1D and 1E). These tumors showed a high proliferative index (Ki67), robust expression of glioma markers (Nestin, GFAP), strong pAKT, and p53DN expression (Figure 1F). These de novo tumors readily generated iGSCs as evidenced by (1) tumor-repopulating potential with as few as 200 implanted cells and median tumor latency of 15–35 weeks (Figure S1C); (2) robust Nestin expression; and (3) limited capacity to differentiate into astrocytic and neuronal lineages (Figure S1D). Accordingly, transduction of c-Myc, p53DN, and myr-AKT in another primary human NSC line also generated high-grade gliomas following intracranial implantation (data not shown). Thus, p53 neutralization and AKT activation cooperate to transform these hNSCs into high-grade gliomas with classical disease features.

To gain mechanistic insight into system-level differences between premalignant hNSCs and their malignant derivatives, we performed transcriptomic analysis focusing on the changes of 68 stem cell-related signaling pathways from Molecular Signatures Database (MSigDB) (Subramanian et al., 2005). Notably, gene set enrichment analysis (GSEA) revealed that upregulation of EC signaling pathway was observed in p53DN-AKT induced transformation of hNSCs (Figures 1G and 1H). Furthermore, genome-wide chromatin immunoprecipitation sequencing (ChIP-seq) analysis focusing on H3K27 histone modifications in core promoter regions revealed 85 genes displaying a dynamic switch from H3K27 trimethylation (me3) to H3K27 acetylation (ac), indicating epigenetic activation during oncogenic transformation of hNSC (Figures 1I and S1E; Table S1). Interestingly, EC signaling pathway, but not HEMATOPOIESIS_STEM_CELL NUMBER_LARGE_VS_TINY_UP ($p > 0.14$), was significantly enriched ($p < 0.05$) in these genes, further highlighting the upregulation of EC signaling pathway in glioma-relevant biological processes. Given the seminal finding that GSCs can differentiate into ECs and participate in tumor vascularization (Ricci-Vitiani et al., 2010; Wang et al., 2010), the above transcriptomic and epigenomic analyses prompted us to verify EC differentiation in our system experimentally. Fluorescence-activated cell sorting (FACS) analysis of EC markers revealed that 12.8% and 8.5% of iGSCs under NSC culture conditions expressed VE-Cadherin

(C) Kaplan-Meier survival analysis for oncogenic transformation of hNSC in vivo.
(D) Representative H&E image of intracranial tumor derived from p53DN-AKT-hNSCs; scale bars, 1 mm.
(E) Representative H&E image of tumor sections with necrotic area (N) and microvascular hyperplasia (black arrow). Scale bars, 50 μm.
(F) IHC staining of tumors with the indicated antibodies. Scale bars, 50 μm.
(G) Top ten signaling pathways related to hNSC oncogenic transformation were identified by GSEA analysis based on gene expression profiles of hNSCs and their derivative cells. The normalized enrichment scores (ES) and the log transformed p values are shown.
(H) GSEA enrichment plots of genes ranked based on oncogenic transformation versus EC signaling pathway.
(I) Heatmap of histone landscape of gene transcriptional start sites (TSSs) within ±2 kb and of Log2-ratio of these gene expression levels in hNSCs and iGSCs.
See also Figure S1 and Table S1.

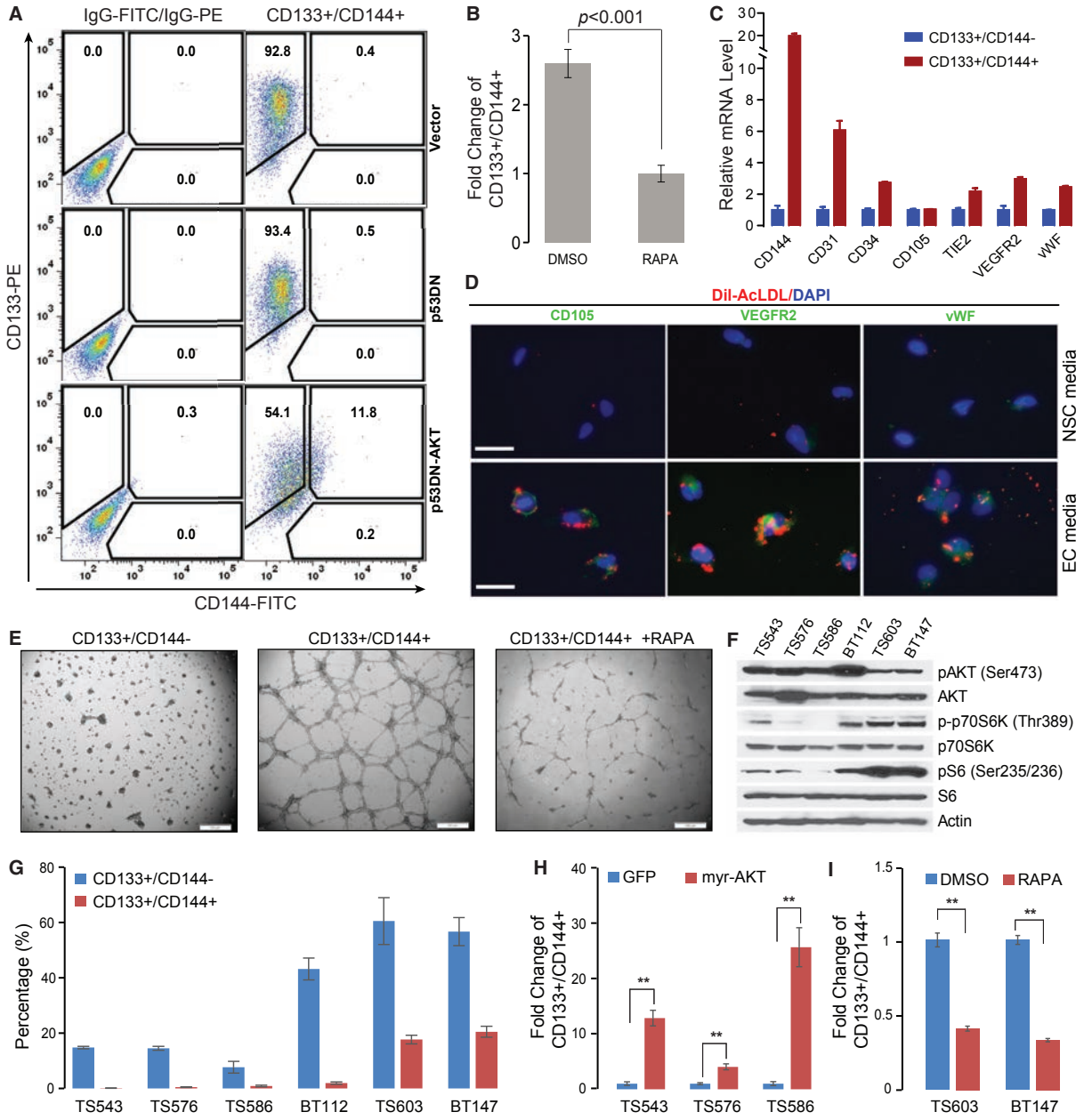

Figure 2. Activation of AKT Pathway Induces Differentiation of GSCs into ECs

(A) FACS analysis of hNSCs, p53DN-transduced hNSCs, and p53DN-AKT-hNSCs based on CD133 and CD144 expression.

(B) Fold change of percentage of CD133$^+$/CD144$^+$ cells by FACS analysis in p53DN-AKT-hNSCs under treatment with rapamycin (RAPA, 50 nM) for 72 hr.

(C) qRT-PCR for indicated EC markers expression in two sorted subpopulations from p53DN-AKT-hNSCs.

(D) IF analysis of sorted CD133$^+$/CD144$^+$ from p53DN-AKT-hNSCs cultured under NSC or EC media for 5 days for EC markers expression and DiI-AcLDL uptake. Scale bar, 40 μm.

(E) Tubular networks formation of sorted CD133$^+$/CD144$^+$ and CD133$^+$/CD144$^-$ cells from p53DN-AKT-hNSCs cultured on Matrigel in EC media with/without RAPA (50 nM) treatment. Scale bar, 100 μm.

(F) Immunoblot analysis of AKT/mTOR pathway activation in patient-derived GSCs.

(legend continued on next page)

(CD144) and PECAM-1 (CD31), respectively (Figure S1F). Moreover, these iGSCs also displayed high levels of classical EC markers and possessed functional EC features such as fluorescent acetylated-low density lipoprotein (DiI-AcLDL) uptake under EC culture conditions (Figures S1G and S1H). Consistently, we also observed GdECs in tumors derived from p53DN-AKT-hNSCs (Figure S1I). Together, these findings of an EC signature and phenotypic features establish that GSC can differentiate into EC in our model system.

AKT Activation Plays a Key Role in Endothelial Lineage Differentiation of GSC

The association of AKT activation in hNSC transformation and EC signature enrichment prompted us to directly assess the potential role of AKT in driving EC differentiation. To that end, immunofluorescence (IF) analysis showed that NSCs expressing p53DN plus myr-AKT, but not p53DN alone, expressed CD144 and CD31 (Figure S2A). Correspondingly, FACS analysis showed that p53DN-AKT-hNSCs expressed CD133 and CD144, which together are known to mark GSC-derived endothelial progenitor cells (Wang et al., 2010); in contrast, p53DN-hNSCs expressed CD133 but not CD144 (Figure 2A). Finally, pharmacological inhibition of AKT signaling with mTOR inhibitor rapamycin decreased the percentage of $CD133^+/CD144^+$ cells in vitro. (Figure 2B).

To reinforce the link between $CD133^+/CD144^+$ cells and EC biology, p53DN-AKT-hNSCs were sorted into $CD133^+/CD144^-$ and $CD133^+/CD144^+$ subpopulations. Compared to $CD133^+/CD144^-$ cells, $CD133^+/CD144^+$ cells showed significantly higher expression levels of CD31, CD34, TIE2, VEGFR2, and von Willebrand factor (vWF) by qRT-PCR (Figure 2C). On the functional level, culturing $CD133^+/CD144^+$ cells in EC media for 5 days resulted in DiI-AcLDL uptake in cells expressing CD105, VEGFR2, and vWF (Figures 2D and S2B), which was also inhibited by rapamycin (Figure S2C). Moreover, when grown in matrigel cultures, $CD133^+/CD144^+$ cells, but not $CD133^+/CD144^-$ cells, were able to form tubular networks and displayed DiI-AcLDL uptake (Figures 2E and S2D), which was abolished by rapamycin (Figure 2E). Importantly, transcriptomic analysis revealed that the level of the EC signature from MSigDB exhibited a stepwise increase in these sorted cell fractions, from $CD133^-/CD144^-$ to $CD133^+/CD144^-$ to $CD133^+/CD144^+$ to $CD133^-/CD144^+$, progressing toward the signature of bona fide endothelial cells (Figure S2E; Table S2). This stepwise differentiation process was further validated in these sorted subpopulations by IF staining of VEGFR2 and endothelial nitric oxide synthase (eNOS), which play important roles in vasculature biology (Förstermann and Münzel, 2006) (Figure S2F).

We further tested whether the level of activated AKT downstream signaling in patient-derived GSCs correlated with EC differentiation. Analysis of six GSC lines showed that two lines with relatively higher pS6 expression (TS603, BT147) exhibited a higher percentage of $CD133^+/CD144^+$ cells (Figures 2F and 2G) and showed considerably greater tube-forming ability (Figure S2G). In contrast, three lines with lower levels of activated AKT downstream signaling (TS543, TS576, and TS586) had lower percentages of $CD133^+/CD144^+$ cells (Figures 2F and 2G). Enforced myr-AKT expression in these three GSC lines significantly increased the fraction of $CD133^+/CD144^+$ cells (Figure 2H). Reciprocally, rapamycin inhibition of AKT pathway decreased the fraction of $CD133^+/CD144^+$ cells in TS603 and BT147 cells (Figure 2I). Together, these results indicate that robust AKT activation plays a key role in driving GSC differentiation with EC-like properties.

AKT Activation Upregulates WNT5A to Drive GdEC Differentiation of GSC

Given the key role of AKT activation in the transformation of hNSCs and endothelial lineage differentiation of GSC, coupling with the association of high-AKT activation with poor prognosis (Suzuki et al., 2010), we identified a list of genes associated with high AKT activation from our oncogene-induced hNSC system (Table S3). To identify genes mediating AKT-induced endothelial lineage differentiation, we intersected these high AKT-associated genes with 85 genes displaying histone modification switch from H3K27me3 to H3K27ac, known to play a pivotal role in lineage commitment and cell fate determination (Adam et al., 2015). Thus, we identified eight upregulated genes (CXCL14, DLX5, DMRT3, GPR37, MYLIP, NUDT14, TCF7, and WNT5A) that might be involved in promoting endothelial lineage differentiation.

To explore this supposition, each gene was transduced into p53DN-hNSCs and monitored for generation of $CD133^+/CD144^+$ cells. Compared to myr-AKT, only WNT5A and DLX5 overexpression generated a considerable percentage of $CD133^+/CD144^+$ cells in p53DN-hNSCs (Figures 3A and 3B). Conversely, small hairpin RNA (shRNA)-mediated knockdown of the eight genes showed that only WNT5A knockdown substantially impaired tubular network formation of $CD133^+/CD144^+$ cells sorted from p53DN-AKT-hNSCs (Figures 3C and 3D). Notably, myr-AKT also dramatically increased WNT5A expression (Figures S3A and S3B). Furthermore, the WNT5A antagonist, BOX5, significantly inhibited the production of $CD133^+/CD144^+$ cells in p53DN-hNSCs transduced with myr-AKT or WNT5A (Figures 3E, S3C, and S3D). Finally, BOX5 treatment blocked tubular network formation of $CD133^+/CD144^+$ cells sorted from p53DN-AKT-hNSCs (Figures 3F, 3G, and S3E). Together, these results indicate that AKT-mediated upregulation of WNT5A plays a pivotal role in the GdEC differentiation of GSC.

Regulation of WNT5A Expression by the Opposing Actions of DLX5 and PAX6

Chromatin landscape and transcriptome comparisons between hNSCs and iGSCs established that, in hNSCs with no WNT5A expression, the WNT5A promoter exhibited a poised (bivalent)

(G) FACS analysis of $CD133^+/CD144^+$ cells in the indicated GSCs.
(H) FACS analysis of $CD133^+/CD144^+$ cells in the indicated GSCs with myr-AKT overexpression.
(I) FACS analysis of $CD133^+/CD144^+$ cells in the indicated GSCs treated with RAPA (50 nM) for 72 hr.
Error bars represent SD of the mean of two (C and G) or three (B, H, and I) independent experiments. $^{**}p < 0.01$. See also Figure S2 and Table S2.

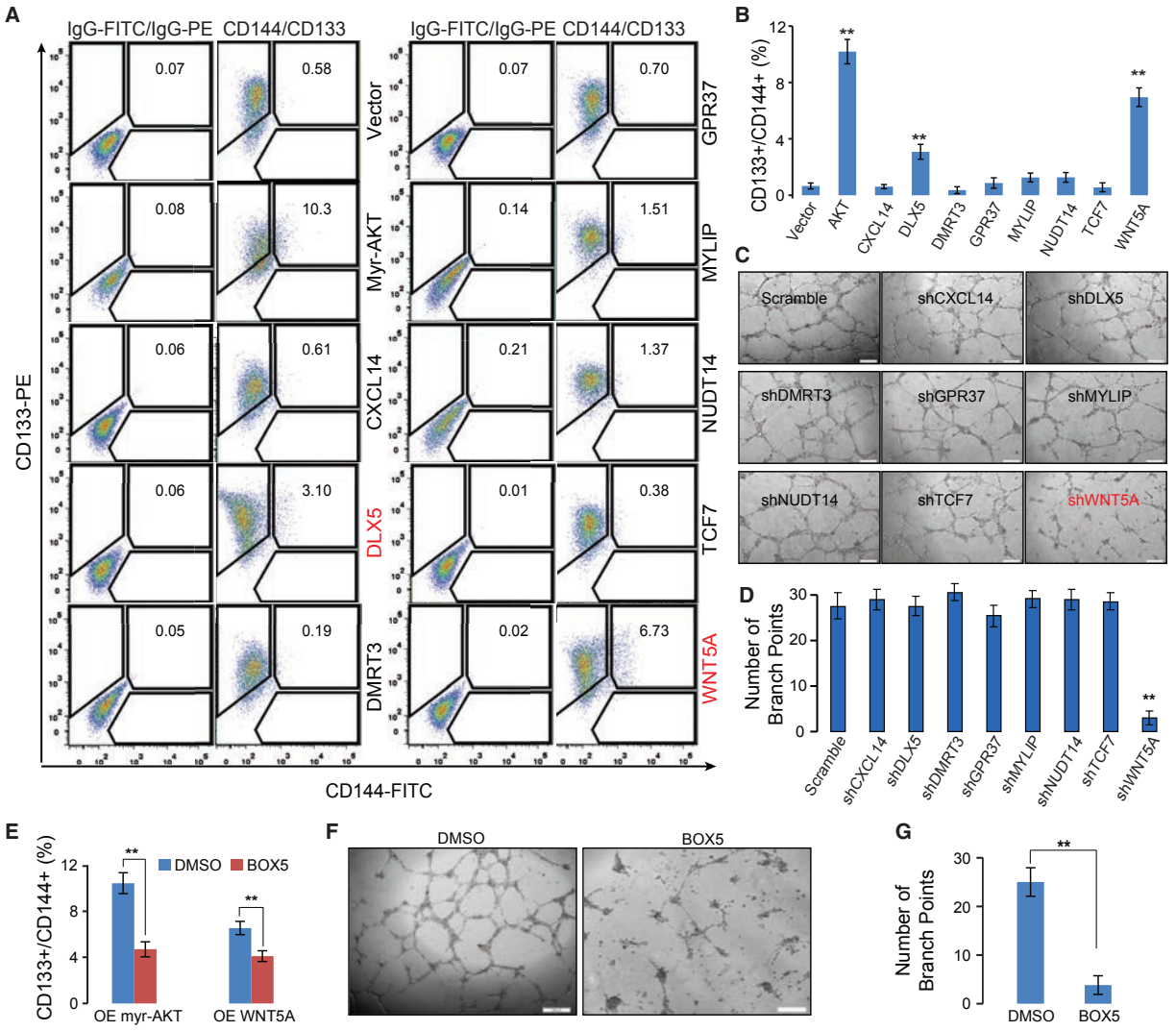

Figure 3. AKT-Driven WNT5A Upregulation in GdECs Differentiation of hNSCs

(A) FACS analysis for the percentage of $CD133^+/CD144^+$ cells in7 days post-infection p53DN-hNSCs cells by lentivirus carrying the indicated genes individually.

(B) Quantitation of the percentage of $CD133^+/CD144^+$ cells in (A) from four independent experiments.

(C) Matrigel tubular network formation of the sorted $CD133^+/CD144^+$ cells from p53DN-AKT-hNSCs with infection by lentivirus carrying pooled short hairpins (minimum three shRNAs) targeting each indicated gene.

(D) Quantitation of the number of tubular networks branch points in (C) (n = 5).

(E) FACS analysis of $CD133^+/CD144^+$ cells in p53DN-hNSCs overexpressing myr-AKT or WNT5A with BOX5 treatment (50 μM) for 72 hr. (n = 3).

(F) Representative images for the tubular network of sorted $CD133^+/CD144^+$ cells from p53DN-AKT-hNSCs with BOX5 treatment. Scale bar, 100 μm.

(G) Number of branch points calculated in (F) (n = 5). Error bars represent SD of the mean; **p < 0.01.

See also Figure S3 and Tables S1 and S3.

chromatin status defined by both H3K4me3 and H3K27me3 marks (Bernstein et al., 2006; Figures 4A, 4B, S3A, and S3B). In contrast, the WNT5A promoter of WNT5A-expressing iGSCs exhibited an active H3K27ac mark with concomitant loss of the repressive H3K27me3 mark (Figures 4A and 4B). These patterns are consistent with the poised WNT5A promoter being epigenetically activated during transformation.

To further explore the mechanisms governing the transcriptional regulation of the WNT5A locus under AKT activation, TCGA proteomic datasets analyses (RPPA) further confirmed the correlation between WNT5A mRNA levels and the mTOR/S6K pathway (Figure S4A). We next identified a significant negative correlation between WNT5A expression and known master transcription factors of NSC self-renewal and lineage

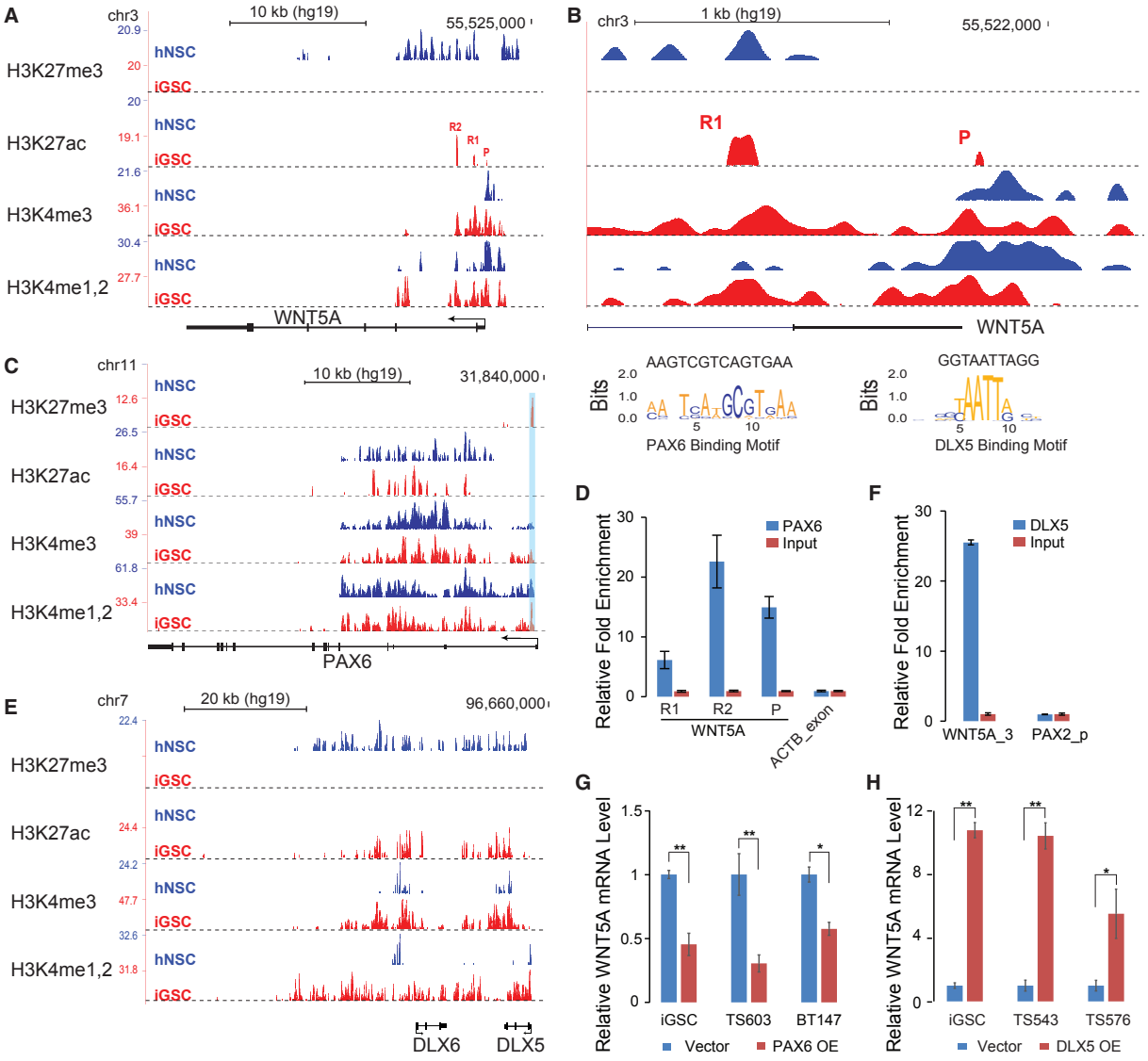

Figure 4. Transcriptional Activation of WNT5A by PAX6 and DLX5

(A) ChIP-seq analysis of chromatin status for WNT5A locus around TSS in hNSC and iGSC.

(B) PAX6 and DLX5 binding motifs in WNT5A regulatory regions.

(C) Chromatin modification changes from hNSC to iGSC for PAX6. The peak of H3K27me in iGSC is highlighted in sky blue color.

(D) Binding of PAX6 in WNT5A regulatory regions in hNSC by ChIP-PCR. Beta-actin locus (ACTB_exon) was used as the negative control (n = 3).

(E) Chromatin modification changes from hNSC to iGSC in DLX5-DLX6 locus.

(F) Binding of DLX5 in WNT5A regulatory regions by ChIP-PCR. PAX2 was used as the control for non-specific binding (n = 3).

(G) WNT5A expression by qRT-PCR analysis in GSCs and iGSC-overexpressing PAX6 (n = 3).

(H) WNT5A expression by qRT-PCR analysis in GSCs and iGSC-overexpressing DLX5 (n = 3). Error bars represent SD of the mean; *$p < 0.05$ and **$p < 0.01$. See also Figure S4.

determination including Gli2, FoxG1, SOX2, PAX4/6, and HES1 in this specific context (Figure S4A). These findings indicate that downregulating the neurogenesis TFs may be necessary for EC lineage differentiation of GSC. Moreover, only the PAX subclass (PAX4 and PAX6) promoter exhibited a gain in repressive H3K27me3 mark following transition from hNSCs to iGSCs (Figures 4C and S4B–S4G). Correspondingly, the WNT5A locus possesses PAX6 binding motifs located in regulatory region 1 (R1), regulatory region 2 (R2), and promoter region (P) (Figures 4A and 4B), which were further validated by ChIP-PCR in hNSCs

(Figure 4D). Consistent with implied negative regulation of PAX6 on WNT5A expression, $CD133^+/CD144^+$ cells sorted from iGSCs showed negligible PAX6 and high WNT5A expression compared to $CD133^+/CD144^-$ cells (Figure S4H).

As noted previously, enforced DLX5 expression in p53DN-hNSCs produced $CD133^+/CD144^+$ cells (Figures 3A and 3B). Notably, the WNT5A promoter possesses a DLX5 binding motif in close proximity to the PAX6 binding site (Figure 4B). Intriguingly, the locus harboring DLX5 exhibited a poised pattern in hNSCs and switched to an epigenetically activated pattern in iGSCs (Figure 4E). ChIP-PCR validated DLX5 binding to the WNT5A promoter region in these iGSCs (Figure 4F). Finally, we solidified PAX6 and DXL5 in the opposing regulation of WNT5A by demonstrating that enforced PAX6 expression reduced WNT5A mRNA and protein levels (Figures 4G and S4I), whereas enforced DLX5 expression increased WNT5A mRNA and protein levels in iGSCs and patient-derived GSCs (Figures 4H and S4J).

In line with our experimental observations, analysis of TCGA GBM gene expression and proteomic profiles showed that WNT5A and DLX5 were positively associated, and PAX6 negatively associated, with activation of the mTOR/S6K pathway (Figure S4A). These results support the view that both PAX6 and DLX5 are repressed and activated, respectively, in response to AKT signaling leading to an epigenetic switch of the WNT5A locus, its transcriptional activation in GSC, and promotion of GdEC differentiation of GSC. These results also align with our observation that DLX5 silencing alone did not impair tubular network formation of GdECs (Figures 3C and 3D), indicating that both the opposite actions of DLX5 and PAX6 are necessary to regulate WNT5A-mediated GdEC differentiation of GSC. We propose that AKT activation upregulates WNT5A, which promotes EC proliferation and differentiation in neovascularization (Cheng et al., 2008; Masckauchán et al., 2006; Yang et al., 2009), thus enabling GSC aberrant developmental plasticity and differentiation into GdEC (Figures S4K and S4L).

WNT5A-Mediated Endothelial Differentiation of GSCs in Tumor Invasive Growth

To address whether WNT5A-mediated endothelial differentiation of GSCs plays a functional role in gliomagenesis in vivo, we next employed a patient-derived GSC orthotopic tumor model that would be more directly relevant to the human pathological condition. TS543 GSC derived tumors had higher levels of PAX6 and lower levels of pS6, WNT5A, and DLX5 compared with GBMs derived from p53DN-AKT-hNSCs (Figure S5A). In the TS543 model, enforced WNT5A expression (WNT5A-TS543) generated tumors with more rapid growth and shorter latency relative to Vector-TS543 controls (Figures S5B–S5D). WNT5A-TS543 gliomas were highly hemorrhagic (Figure 5A), showed increased microvascular density (MVD) and exhibited increased expression of endothelial markers (Figures 5A, S5E, and S5F). WNT5A-TS543 gliomas were strikingly more invasive, generating many distant satellite lesions in the peritumoral brain parenchyma that were evident on histologic examination (Figure S5G) and confirmed by human-specific antigen (TRA-1-85/CD147) IF staining (Figures 5B and S5H). Finally, WNT5A promoted endothelial differentiation in vivo as evidenced by increased $CD34^+/TRA\text{-}1\text{-}85^+$ GdECs in the intratumoral and peritumoral regions of gliomas derived from WNT5A-TS543 (Figures 5C and 5D). Of note, there was a higher number of GdECs in the peritumoral regions compared to intratumoral regions (Figures 5C–5E). Thus, WNT5A drives GdEC differentiation, which is associated with an increase in tumor neovascularization and an increase in peritumoral satellite lesions, which may provide a microenvironment to promote the growth of invading glioma cells throughout the brain parenchyma.

To ascertain the tumor biological significance of these WNT5A-mediated phenotypes, the herpes simplex virus thymidine kinase gene (HSVTK)/ganciclovir (GCV) cell ablation system was used to selectively eliminate GdECs in vivo. To that end, we constructed a vector encoding an HSVTK-GFP fusion protein under control of the CD144 promoter (hereafter, *p*CD144-GFP) (Figure S5I). Following *p*CD144-GFP transduction into TS543 and WNT5A-TS543 GSCs, FACS detected 0.61% and 6.98% GFP^+ cells, respectively (Figures S5J and S5K). Next, 1 week following orthotopic implantation of *p*CD144-GFP-transduced WNT5A-TS543 GSCs, mice were treated with GCV resulting in increased apoptosis in *p*CD144-GFP^+ GdECs relative to controls (Figure S5L). Tumors from GCV-treated animals showed overall reduction in intratumoral MVD detected by CD34 staining and a modest increase in mouse survival (Figures 5F, 5G, and S5M). Notably, while the depletion of GdECs by GCV showed similar intratumoral size, it dramatically decreased satellite lesions and invasiveness in peritumoral areas (Figures 5H and S5N), supporting a key role for GdECs in tumor invasive growth.

WNT5A-Mediated GdECs Recruitment of Non-transformed ECs Promotes GSCs Self-Renewal and Invasive Growth

We next investigated the role of GdECs in peritumoral satellite lesion formation with a specific emphasis on whether these peritumoral satellite lesions might support the growth of invading glioma cells in the periphery. We observed that the higher frequency of GdECs in tumors derived from *p*CD144-GFP-transduced WNT5A-TS543 correlated with higher MVD. Moreover, host mouse ECs ($CD34^+/TRA\text{-}1\text{-}85^-$) were in close proximity to GdECs in peritumoral areas (Figures 6A, 6B, and S6A–S6C), raising the possibility that GdECs may recruit host ECs to form peritumoral satellite lesions. To assess this possibility, we performed transwell assays using GdECs sorted from *p*CD144-GFP-transduced WNT5A-TS543 and GSC TS603 (endogenous WNT5A), respectively, and demonstrated increased recruitment of human brain microvascular endothelial cells (HBMECs) compared with non-GdECs sorted from these GSCs (Figures 6C and 6D). Furthermore, WNT5A mRNA levels were higher in GdECs subpopulations than non-GdEC subpopulations sorted from *p*CD144-GFP-transduced WNT5A-TS543 and GSC TS603 cultures (Figure 6E). We next determined whether WNT5A directly mediates EC recruitment. In the transwell assay, recombinant WNT5A (rWNT5A), but not rWNT3A, acted as a chemoattractant and significantly recruited HBMECs, which was drastically impaired in the presence of WNT5A antagonist BOX5 (Figure 6F). Importantly, WNT5A increased HBMECs proliferation and survival in serum-free medium (Figure S6D). Together, these results indicate that GdECs-derived WNT5A can stimulate EC recruitment and proliferation. Furthermore, in

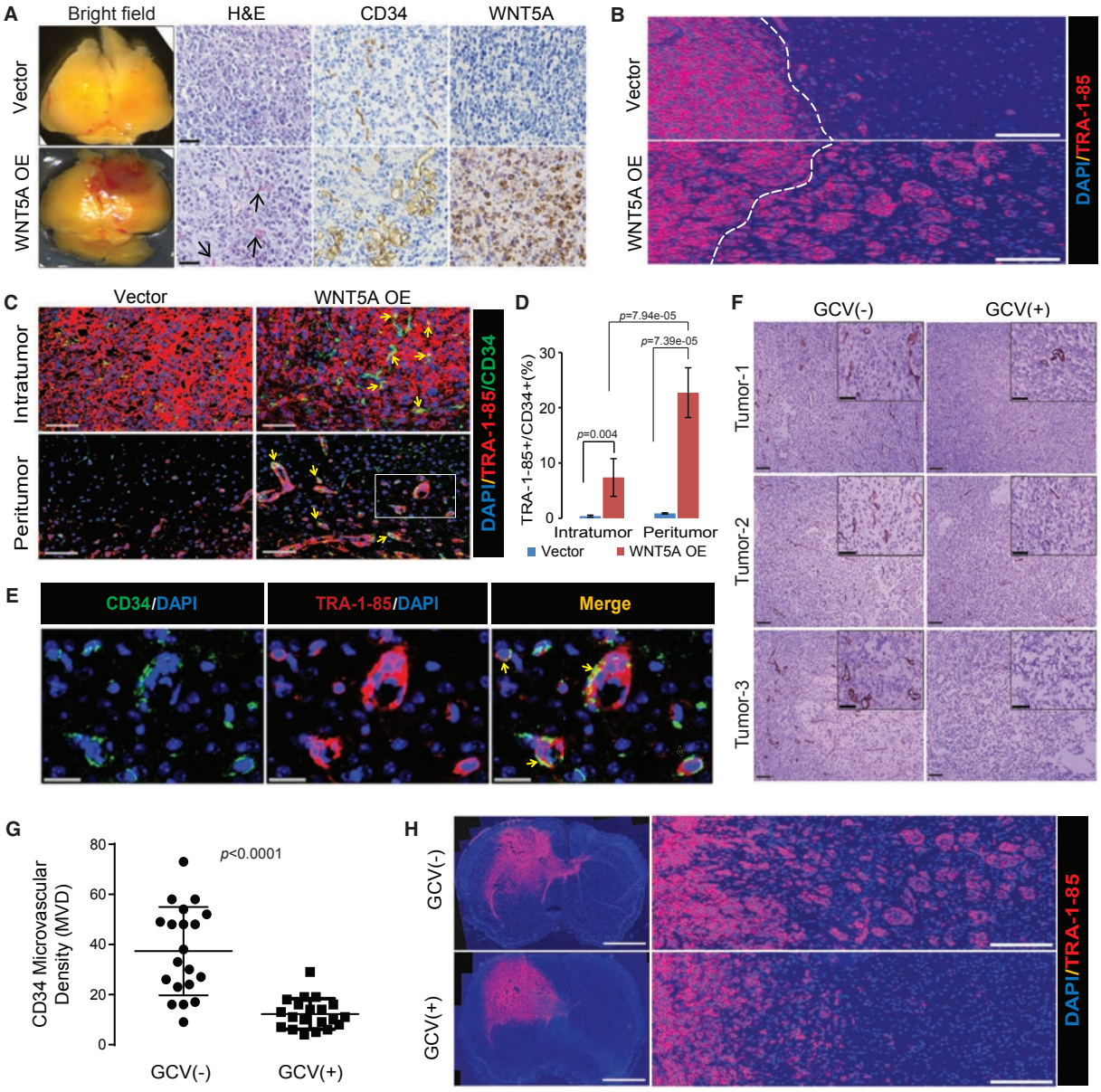

Figure 5. WNT5A-Mediated Endothelial Lineage Differentiation in Tumor Neovascularization and Satellite Lesion Formation

(A) Representative images for the hemorrhage lesion in mouse brain that received injection of TS543-overexpressing WNT5A (WNT5A OE) versus control (Vector). H&E and IHC analyses of tumor sections show the microvascular hyperplasia (black arrows) and expression of CD34 and WNT5A. Scale bar, 50 μm.

(B) Representative images for the satellite lesions in peritumoral areas. Scale bar, 200 μm.

(C) Representative images for GdECs (yellow arrows) identified by co-staining with TRA-1-85 and CD34 in intratumoral and peritumoral areas. Scale bar, 25 μm.

(D) Quantitation of TRA-1-85$^+$/CD34$^+$ cells using Vectra software system (n = 3 tumors).

(E) High magnification of rectangle area in (C). Scale bar, 10 μm.

(F) IHC staining of CD34 in intracranial tumors derived from*p*CD144-GFP infected WNT5A-TS543following GCV treatment. Representative images of low (scale bar, 100 μm) and high (scale bar, 50 μm) magnification.

(G) Dotplots for quantitation of MVD in tumors with/without GCV treatment (n = 4 tumors, five fields per tumor).

(H) Representative images for tumor appearance (left, scale bar, 2,000 μm) and peritumoral satellite lesions (right, scale bar, 200 μm).

See also Figure S5.

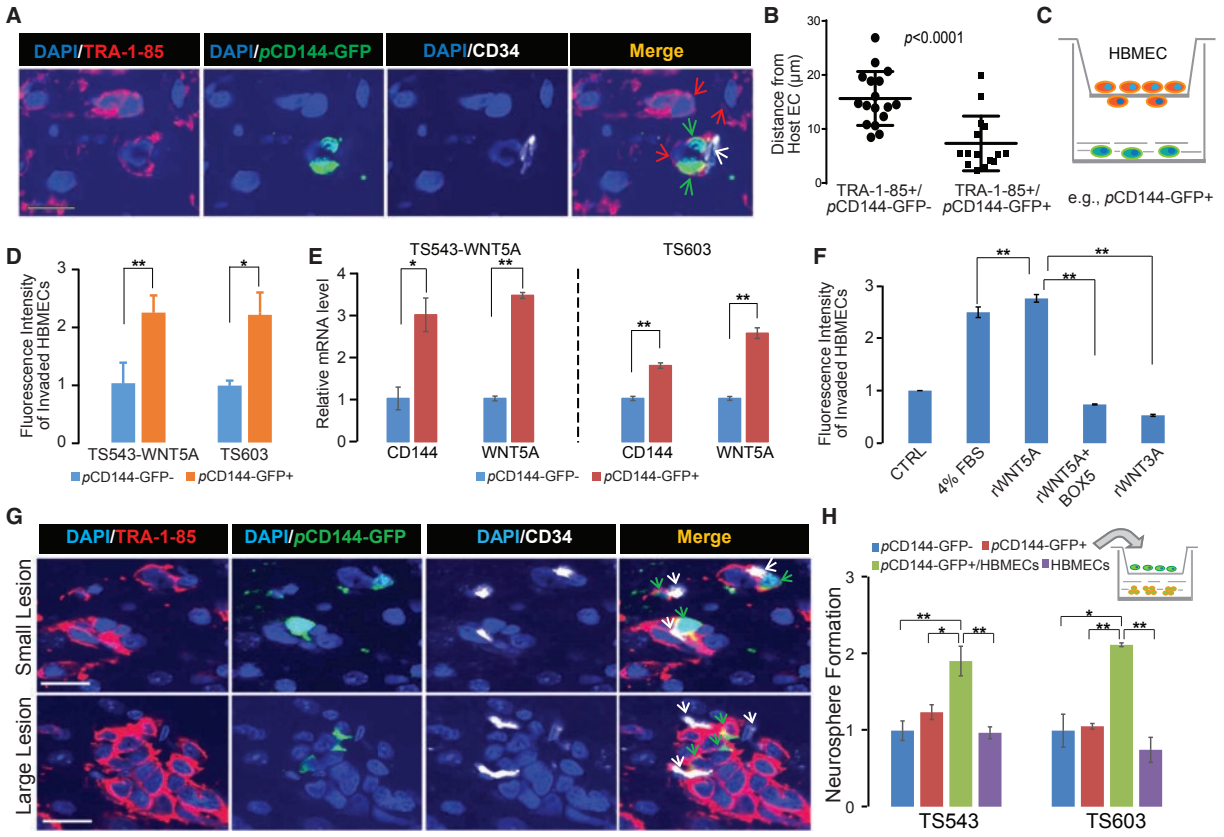

Figure 6. Recruitment of Host ECs by WNT5A-Mediated GdECs Contributes to GSCs Self-Renewal and Proliferation

(A) Representative images of IF analysis for GdECs (green arrows), compared with tumor cells (red arrows), are in close proximity to mouse ECs (white arrow) in tumor sections. Scale bar, 10 μm.

(B) Dotplots show the distance from mouse ECs to the nearest tumor cells and GdECs, respectively (n ≥ 15).

(C) Illustration of the transwell system to measure EC recruitment.

(D) Fluorescence intensity shows HBMECs recruitment after co-culture with GdECs for 24 hr (n ≥ 3).

(E) qRT-PCR for CD144 and WNT5A mRNA levels in sorted *p*CD144-GFP$^-$ and *p*CD144-GFP$^+$ from TS543-WNT5A and TS603 (n = 3).

(F) Fluorescence intensity shows HBMECs recruitment after co-culture with NSC media containing rWNT5A (0.5 μg/ml) or rWNT3A (0.05 μg/ml) (n = 3).

(G) Representative images of GdECs (green arrows) and mouse ECs (white arrows) in variously sized satellite lesions. Scale bar, 20 μm.

(H) Neurosphere formation of TS543 or TS603 co-cultured with GdECs and HBMECs (n = 3). Cartoon depicting the experimental approach. Error bars represent SD of the mean; *p < 0.05 and **p < 0.01.

See also Figure S6.

GBM sections, *p*CD144-GFP$^+$ GdECs were consistently in close proximity to host ECs (CD34$^+$/TRA-1-85$^-$) in the peritumoral satellite lesions; and the larger satellite lesions possessed greater numbers of GdECs and mouse host ECs (Figure 6G). Additionally, GCV-mediated depletion of GdECs resulted in diminished satellite lesion formation (Figure 5H), although individual SOX2 positive GSCs were still present throughout peritumoral area (data not shown). These observations suggest that GdECs are required for the maintenance and expansion of the peritumoral satellite lesions, prompting us to speculate that GdECs recruit host ECs, which may act synergistically to provide a microenvironment that supports the growth and survival of GSCs in these peritumoral areas. To test this hypothesis, we audited tumor sphere formation to check proliferation and self-renewal of GSCs in the presence of GdEC + HBMEC co-cultures. Strikingly, only GdEC/HBMEC co-cultures, but not GdEC or HBMEC cultures, increased sphere formation of GSC TS543 and TS603 (Figures 6H and S6E). These co-cultures also increased soft agar colony formation of TS543 and TS603 (Figures S6F and S6G). These observations gain added significance in light of emerging evidence for the crucial role of ECs in NSC/GSC niche formation that supports NSC/GSC growth and survival (Calabrese et al., 2007; Shen et al., 2004; Zhu et al., 2011). Together, these observations support our model that GSC differentiation into GdEC stimulates host EC recruitment via WNT5A to create a vascular-like niche supporting GSC growth and survival, thereby promoting tumor cells growth beyond the primary tumor microenvironment.

WNT5A-Mediated GdEC in Human GBM Recurrence

To investigate the clinical relevance of our findings, we asked whether the WNT5A-mediated process of GdEC biology is operative in GBM patient specimens. First, we documented that WNT5A mRNA levels were significantly higher in GBM tumors than in non-tumor brain tissues (Figure S7A). Second, we documented the presence of GdECs ($SOX2^+/CD31^+$, $SOX2^+/CD105^+$, or $CD133^+/CD31^+$) and established a significant correlation between high WNT5A expression and increasing frequency of GdECs in human GBMs (Figures 7A, S7B, and S7C). Moreover, GdECs were noted to situate close to host ECs ($SOX2^-/CD31^+$, $SOX2^-/CD105^+$, or $CD133^-/CD31^+$) (Figure 7A), which was verified by objective proximity measurements of GdECs and host EC in tumor sections that were double-stained (immunohistochemistry [IHC]) and assessed by an automated quantitative pathology imaging system (Figures 7B and 7C). To further verify these findings in large-scale human GBM datasets, we generated a GdEC signature by integrated analyses of transcriptomic profiling from our de novo GBM model and EC signature from MSigDB, which included genes upregulated in both neoplastic and the EC signaling process (Tables S2 and S4). Based on 364 primary IDHwt GBM from TCGA datasets, we found that both GdEC and EC signatures were positively associated with WNT5A mRNA expression (Figures 7D and S7D). Together, these human GBM data strongly align with our experimental findings of WNT5A-directed GdEC differentiation and associated host EC recruitment in GBM.

As shown in previous studies (Ricci-Vitiani et al., 2010; Wang et al., 2010), we observed that GdEC ($SOX2^+/CD31^+$) was incorporated into blood vessels in human GBM tumor sections (Figure S7E). Importantly, we observed (1) peritumoral satellite lesions in GBM patient samples, (2) GdECs ($CD31^+/SOX2^+$) in close proximity to host ECs ($CD31^+/SOX2^-$) in these structures, (3) larger satellite lesions possessed greater numbers of GdECs and host ECs (Figures 7E and 7F). To investigate whether WNT5A expression is associated with peritumoral satellite lesions and patient outcome, 14 primary GBMs with progression-free survival (PFS) information were stained for WNT5A, revealing that higher levels of WNT5A were associated with increased number of peritumoral satellite lesions and with a tendency to develop recurrent tumors with a shorter PFS (Figures 7G and S7F). Strikingly, using transcriptomic profiling from a previous study (Sottoriva et al., 2013), we found that WNT5A and GdEC signature are significantly higher in the peritumoral regions compared with matched intratumoral regions for GBM patients (Figures 7H and S7G). Using another RNA-seq dataset from previous study (Gill et al., 2014), we observed a dramatic increase of WNT5A expression and GdEC signature in nonenhancing (NE) regions versus contrast-enhancing (CE) regions from 27 different GBM patients (Figures S7H and S7I). These findings reinforce the key role of WNT5A and GdEC in the peritumoral disease and support the mechanism of their cooperative role in disease recurrence. Furthermore, multiple variable COX analysis clearly demonstrates that WNT5A is an independent prognostic factor for PFS in GBM patients (Figure 7I; Tables S5 and S6).

To validate WNT5A/GdEC in tumor recurrence, 14 paired primary/recurrent GBMs tumor sections were immunohistochemically stained and showed significantly higher levels of WNT5A and CD31 (marker for GdEC and EC) in recurrent tumors compared to their paired primary tumors (Figures 7J, S7J, and S7K). Furthermore, the significantly higher frequency ($p = 5.5e\text{-}7$) of GdECs at recurrence was systematically and accurately identified by an automated quantitative pathology imaging system (Figure 7K). Most importantly, comprehensive transcriptome analysis on 81 paired primary/recurrent IDHwt GBMs validated increased WNT5A expression and GdEC signature in recurrent GBMs compared to paired primary GBMs (Figures 7L and S7L). Pairwise comparisons also displayed the strong association of both GdEC and EC signature with WNT5A in recurrent GBMs (Figures 7M and S7M). Collectively, these data strongly support our experimental findings that WNT5A-mediated GdEC differentiation contributes to peritumoral satellite lesion formation and tumor recurrence in human GBM (Figure S7N).

DISCUSSION

In this study, we generated a de novo human GBM model enabling precise comparison of chromatin and transcriptomic changes in the malignant transformation of human NSCs into GSCs. Our efforts to understand the mechanisms governing GSC hallmark features and their contributions to GBM's clinical properties resulted in identification of the opposing actions of DLX5 activation and PAX6 repression of WNT5A transcription, which, in turn, drives a differentiation program producing GdECs. Together with recruited host ECs, these GdECs support glioma cell growth and invasion in the surrounding brain parenchyma—tumor biological properties that are intimately associated with glioma recurrence in patients.

Transcriptional regulatory networks known to regulate stem cell plasticity and lineage determination under physiological conditions are shown here to be hijacked to mediate GdEC differentiation of GSC in gliomagenesis. Specifically, our identification and functional validation of WNT5A in this process is consistent with previous work showing that WNT5A can promote embryonic stem cell differentiation into EC lineage during normal vascular development, and can regulate EC proliferation, migration, and survival in angiogenesis (Cheng et al., 2008; Masckauchán et al., 2006; Yang et al., 2009). Interestingly, PAX6 can function as a tumor suppressor and inhibit angiogenesis and invasion in glioma (Mayes et al., 2006; Zhou et al., 2005). Furthermore, DLX5 has been shown to regulate WNT5A expression in CNS development and DLX5 expression has been observed in $CD133^+$ GBM cells (Liu et al., 2009; Paina et al., 2011). Finally, AKT enhances protein stability and transcriptional activity of DLX5 (Jeong et al., 2011); and AKT activation also upregulates CCCTC binding factor, which can epigenetically repress PAX6 transcription via promoter methylation (Gao et al., 2007, 2011). Collectively, these reports along with our findings, strongly substantiate a role of the AKT-DLX5/PAX6-WNT5A axis in regulation of aberrant developmental oncobiology, which plays a key role in GBM's lethal pathophysiology (Figures S4K and S4L).

The frequency and function of GSC differentiation into GdEC have been a source of controversy in the GBM field (Cheng et al., 2013; Ricci-Vitiani et al., 2010; Rodriguez et al., 2012;

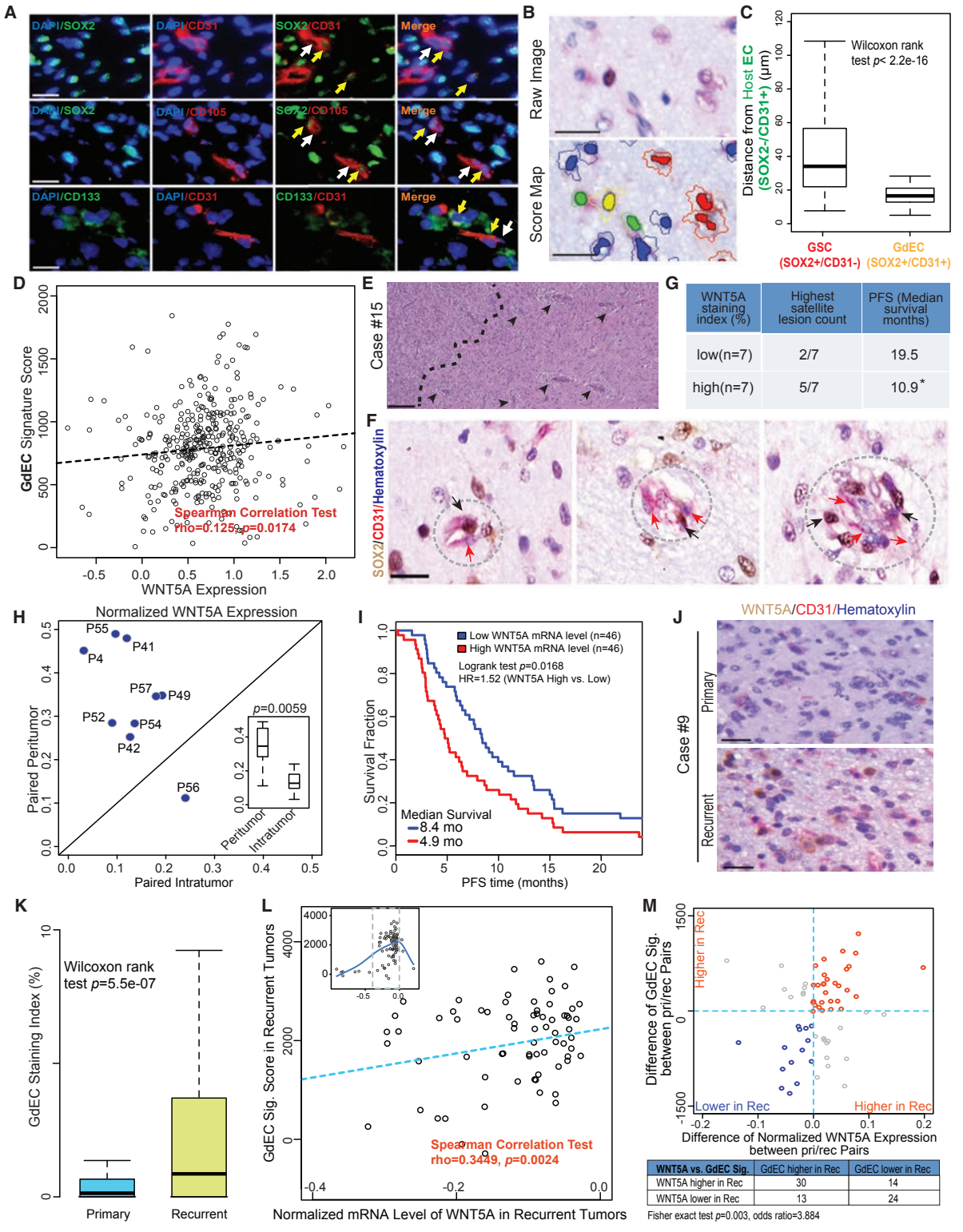

(legend on next page)

Soda et al., 2011; Wang et al., 2010). Our work provides reinforcing evidence of this phenomenon and expands our understanding of the molecular underpinnings and tumor biological relevance of GdECs. Specifically, as a result of AKT activation, GdECs produce WNT5A resulting in recruitment and proximal association of host ECs, which, in turn, promotes distant satellite lesion formation and glioma cell invasive growth. The sources of host ECs in our model remain to be determined and may include circulating endothelial cells and bone-marrow-derived endothelial progenitor cells (Boer et al., 2014; Folkins et al., 2009), in additional to a dense network of microvasculature within the brain. Importantly, we found that GdECs not only recruit host ECs, but also increase their proliferation in a WNT5A-dependent manner, a finding that provides a rational explanation for the previous observation of robust neovascularization yet low frequency of GdECs integration into tumor vessels.(Rodriguez et al., 2012). GSCs enrichment has been observed in perivascular and hypoxia niche, which has been shown to maintain GSC multipotency and tumor initiation potential as well as tumor progression, therapeutic resistance, and recurrence (Calabrese et al., 2007; Lathia et al., 2011). However, little is known about how GSCs are maintained outside of these native niches in the peritumoral regions, which can drive disease recurrence following surgery and radiotherapy. Our in vitro and in vivo findings support a model whereby GdECs play an instructive role in establishing a vascular-like niche for GSCs maintenance and growth via WNT5A-mediated recruitment of existing ECs. In particular, we noted that GdECs recruit ECs within very small cell clusters (Figures 6G and 7F), and thus the initiation of neovascularization in GBM may occur prior to the hyperplasia to neoplasia transition (Folkman et al., 1989; Hanahan and Folkman, 1996) and likely independent of hypoxia in these peritumoral areas. Importantly, we observe that GdEC + EC co-cultures are able to enhance GSC self-renewal, which supports their cooperative role in supporting distal tumor invasive growth, hence tumor recurrence.

Clinically, disease recurrence is the sine qua non of GBM with tumor re-emergence typically within a few centimeters of the primary tumor bed following optimal multi-modality treatment (Giese et al., 2003). Based on comprehensive analysis using human GBMs specimens and datasets, our study establishes a strong correlation among elevated levels of WNT5A and GdEC signature, peritumoral satellite lesions, and tumor recurrence, prompting us to speculate that WNT5A-mediated EC differentiation of GSC and satellite lesion formation provide a nurturing tumor microenvironment in the brain parenchyma. In this light, it is worth noting that, while bevacizumab has been approved as a single-agent for recurrent GBM, patients experience only transient benefit and develop highly infiltrative tumors (de Groot et al., 2010; Ferrara et al., 2004). Thus, it would be interesting to explore whether bevacizumab increases WNT5A-mediated endothelial lineage differentiation resulting in these refractory phenotypes. Notably, a previous study showed that GSCs differentiation into ECs failed to be blocked by anti-VEGF inhibitors and that GdECs were increased following VEGF receptor inhibitor treatment in mouse GBM (Soda et al., 2011). On the basis of these clinical and experimental observations, together with mechanistic findings of this study, we propose the therapeutic strategy of targeting WNT5A-mediated GSCs differentiation into ECs and GdECs recruitment of exiting ECs (Figure S7N). This strategy should ameliorate the outcome of GBM patients undergoing VEGF therapy, by limiting tumor neovascularization, invasiveness, and disease recurrence.

STAR★METHODS

Detailed methods are provided in the online version of this paper and include the following:

- KEY RESOURCES TABLE
- CONTACT FOR REAGENT AND RESOURCE SHARING

Figure 7. Correlation of WNT5A-Mediated GdEC with Peritumoral Satellite Lesion and Tumor Recurrence in GBM Patients

(A) Representative images of GdECs (yellow arrows) defined using indicated EC and GSC markers. White arrows denote host ECs. Scale bar, 20 μm.

(B) Representative images with IHC double-staining and cell segmentation obtained from Caliper InForm analysis software show the close proximity of GdEC ($SOX2^+/CD31^+$, yellow) and host ECs ($SOX2^-/CD31^+$, green) compared with GSCs ($SOX2^+/CD31^-$, red) in tumor sections. $SOX2^-/CD31^-$ cells are marked in blue color. Scale bar, 20 μm.

(C) Boxplot of distances from host ECs to the nearest GSCs and GdECs, respectively (n = 300).

(D) The correlation between WNT5A mRNA expression and GdEC signature score. n = 364 (IDHwt GBMs); mRNA expression was normalized across genes.

(E) Representative image of H&E staining for intratumoral and peritumoral regions (black dashed line) of GBM patient's sample. Black arrows denote peritumoral satellite. Scale bar, 200 μm.

(F) Representative images for GdECs (black arrows) and host ECs (red arrows) in variously sized satellite lesions in IHC double-staining tumor sections. Scale bar, 25 μm.

(G) Fourteen patients' primary tumors were divided by WNT5A staining index into two groups (low and high). Tumor sections with peritumoral satellite lesions (more than ten) were counted as the highest score. *p = 0.04 by the log-rank test for PFS between two groups, HR = 3.45 (high versus low).

(H) Comparison of WNT5A mRNA expression between nine pairs of intratumor and peritumor regions from GBM patients. Each dot in the scatterplot represents a pair. Boxplot summarizes the distribution of WNT5A expression in nine intratumor and peritumor regions, respectively.

(I) TCGA GBMs (IDHwt, n = 228) were used for PFS analysis. Red and blue lines show survival curves of top 20% of GBMs with highest and lowest WNT5A mRNA expression, respectively.

(J) Representative images for WNT5A (brown) and CD31 (red) staining of paired primary/recurrent tumors from one GBM patient. Scale bar, 25 μm.

(K) Unbiased quantification of GdEC frequency in primary and recurrent GBMs (n = 150).

(L) Correlation between WNT5A expression and GdEC signature scores in recurrent GBMs. Small boxplot panel shows all 81 pairs while the big boxplot panel shows the majority of samples.

(M) Association of differences of WNT5A mRNA expression and GdEC signature score between 81 matched primary/recurrent GBMs pairs. Each circle in the scatterplot represents a GBM pair; mRNA expression was normalized across genes.

See also Figure S7 and Tables S2, S4, S5, and S6.

SUPPLEMENTAL INFORMATION

Supplemental Information includes seven figures and seven tables and can be found with this article online at http://dx.doi.org/10.1016/j.cell.2016.10.039.

AUTHOR CONTRIBUTIONS

B.H., Y.A.W., and R.A.D. designed the project and analyzed data; B.H. performed the experiments; Q.W. performed bioinformatics analysis for ChIP-seq, RNA-seq, DNA microarray, and clinical datasets; S.H. performed ChIP-seq, DNA microarray, and data analysis; R.G.W.V., Y.Z., and J.Z. provided assistance for TCGA data analysis; C.-E.G.S., D.O., M.M.M., P.D., Y.W.H., G.W., Z.T., H.Y., and W.-T.L. provided assistance in cell-culture and molecular biochemical experiments; Q.C. provided assistance in image capture; Q.W., J.Z., Y.Y., N.L., and L.C. provided assistance for analysis of GBM paired samples; Z.D.L., G.N.F., J.J.P., and M.S.B. provided TCGA GBM biospecimens; E.P.S., G.N.F., and L.J.C. provided assistance for pathological analysis on human GBM samples; L.C. provided intellectual contribution and designed early study. S.H., C.-E.G.S., D.O., X.L., J.H., and D.J.S. provided critical intellectual contributions throughout the project; B.H., Y.A.W., and R.A.D. wrote the manuscript.

ACKNOWLEDGMENTS

The authors thank Dr. Raghu Kalluri for critical reading and comments; Dr. Keith L. Ligon for initial assistance with histopathological analysis and providing GSCs lines; Drs. Colin Watts, Andrea Sottoriva, and Sara G.M. Piccirillo for providing detailed information about their published datasets of gene expression profile; Verlene K. Henry and her staff for their help in mouse brain implantation; Keith A. Michel and Charles V. Kingsley for assistance with MRI imaging and analysis; Shan Jiang for excellent mouse husbandry and care; Dr. Jared K. Burks for assistance with confocal image and PE Vectra system; Dr. Karen C. Dwyer and her staff for assistance with flow cytometer; Sequencing & Non-Coding RNA program and Sequencing and Microarray Facility at MDACC provided sequencing service. This research is supported by UCSF Brain Tumor SPORE Tissue Bank P50 CA097257 (J.J.P.), NIH 2P50CA127001 (YAW), 5P01CA095616 (R.A.D. and L.C.), the Ben and Catherine Ivy Foundation Research Award (2009, R.A.D. and L.C.), and Clayton Foundation (RAD). The core facilities are supported by P30CA16672.

Received: March 22, 2016
Revised: August 11, 2016
Accepted: October 20, 2016
Published: November 17, 2016

REFERENCES

Adam, R.C., Yang, H., Rockowitz, S., Larsen, S.B., Nikolova, M., Oristian, D.S., Polak, L., Kadaja, M., Asare, A., Zheng, D., and Fuchs, E. (2015). Pioneer factors govern super-enhancer dynamics in stem cell plasticity and lineage choice. Nature *521*, 366–370.

Alcantara Llaguno, S., Chen, J., Kwon, C.H., Jackson, E.L., Li, Y., Burns, D.K., Alvarez-Buylla, A., and Parada, L.F. (2009). Malignant astrocytomas originate from neural stem/progenitor cells in a somatic tumor suppressor mouse model. Cancer Cell *15*, 45–56.

Bao, S., Wu, Q., McLendon, R.E., Hao, Y., Shi, Q., Hjelmeland, A.B., Dewhirst, M.W., Bigner, D.D., and Rich, J.N. (2006). Glioma stem cells promote radioresistance by preferential activation of the DNA damage response. Nature *444*, 756–760.

Bernstein, B.E., Mikkelsen, T.S., Xie, X., Kamal, M., Huebert, D.J., Cuff, J., Fry, B., Meissner, A., Wernig, M., Plath, K., et al. (2006). A bivalent chromatin structure marks key developmental genes in embryonic stem cells. Cell *125*, 315–326.

Boer, J.C., Walenkamp, A.M., and den Dunnen, W.F. (2014). Recruitment of bone marrow derived cells during anti-angiogenic therapy in GBM: The potential of combination strategies. Crit. Rev. Oncol. Hematol. *92*, 38–48.

Brennan, C.W., Verhaak, R.G., McKenna, A., Campos, B., Noushmehr, H., Salama, S.R., Zheng, S., Chakravarty, D., Sanborn, J.Z., Berman, S.H., et al.; TCGA Research Network (2013). The somatic genomic landscape of glioblastoma. Cell *155*, 462–477.

Calabrese, C., Poppleton, H., Kocak, M., Hogg, T.L., Fuller, C., Hamner, B., Oh, E.Y., Gaber, M.W., Finklestein, D., Allen, M., et al. (2007). A perivascular niche for brain tumor stem cells. Cancer Cell *11*, 69–82.

Cancer Genome Atlas Research Network (2008). Comprehensive genomic characterization defines human glioblastoma genes and core pathways. Nature *455*, 1061–1068.

Ceccarelli, M., Barthel, F.P., Malta, T.M., Sabedot, T.S., Salama, S.R., Murray, B.A., Morozova, O., Newton, Y., Radenbaugh, A., Pagnotta, S.M., et al.; TCGA Research Network (2016). Molecular profiling reveals biologically discrete subsets and pathways of progression in diffuse glioma. Cell *164*, 550–563.

Chen, J., Li, Y., Yu, T.S., McKay, R.M., Burns, D.K., Kernie, S.G., and Parada, L.F. (2012). A restricted cell population propagates glioblastoma growth after chemotherapy. Nature *488*, 522–526.

Cheng, C.W., Yeh, J.C., Fan, T.P., Smith, S.K., and Charnock-Jones, D.S. (2008). Wnt5a-mediated non-canonical Wnt signalling regulates human endothelial cell proliferation and migration. Biochem. Biophys. Res. Commun. *365*, 285–290.

Cheng, L., Huang, Z., Zhou, W., Wu, Q., Donnola, S., Liu, J.K., Fang, X., Sloan, A.E., Mao, Y., Lathia, J.D., et al. (2013). Glioblastoma stem cells generate vascular pericytes to support vessel function and tumor growth. Cell *153*, 139–152.

de Groot, J.F., Fuller, G., Kumar, A.J., Piao, Y., Eterovic, K., Ji, Y., and Conrad, C.A. (2010). Tumor invasion after treatment of glioblastoma with bevacizumab: Radiographic and pathologic correlation in humans and mice. Neuro-oncol. *12*, 233–242.

Dunn, G.P., Rinne, M.L., Wykosky, J., Genovese, G., Quayle, S.N., Dunn, I.F., Agarwalla, P.K., Chheda, M.G., Campos, B., Wang, A., et al. (2012). Emerging insights into the molecular and cellular basis of glioblastoma. Genes Dev. *26*, 756–784.

Ferrara, N., Hillan, K.J., Gerber, H.P., and Novotny, W. (2004). Discovery and development of bevacizumab, an anti-VEGF antibody for treating cancer. Nat. Rev. Drug Discov. *3*, 391–400.

Folkins, C., Shaked, Y., Man, S., Tang, T., Lee, C.R., Zhu, Z., Hoffman, R.M., and Kerbel, R.S. (2009). Glioma tumor stem-like cells promote tumor

angiogenesis and vasculogenesis via vascular endothelial growth factor and stromal-derived factor 1. Cancer Res. *69*, 7243–7251.

Folkman, J., Watson, K., Ingber, D., and Hanahan, D. (1989). Induction of angiogenesis during the transition from hyperplasia to neoplasia. Nature *339*, 58–61.

Förstermann, U., and Münzel, T. (2006). Endothelial nitric oxide synthase in vascular disease: From marvel to menace. Circulation *113*, 1708–1714.

Furnari, F.B., Fenton, T., Bachoo, R.M., Mukasa, A., Stommel, J.M., Stegh, A., Hahn, W.C., Ligon, K.L., Louis, D.N., Brennan, C., et al. (2007). Malignant astrocytic glioma: Genetics, biology, and paths to treatment. Genes Dev. *21*, 2683–2710.

Gao, J., Li, T., and Lu, L. (2007). Functional role of CCCTC binding factor in insulin-stimulated cell proliferation. Cell Prolif. *40*, 795–808.

Gao, J., Wang, J., Wang, Y., Dai, W., and Lu, L. (2011). Regulation of Pax6 by CTCF during induction of mouse ES cell differentiation. PLoS ONE *6*, e20954.

Giese, A., Bjerkvig, R., Berens, M.E., and Westphal, M. (2003). Cost of migration: Invasion of malignant gliomas and implications for treatment. J. Clin. Oncol. *21*, 1624–1636.

Gill, B.J., Pisapia, D.J., Malone, H.R., Goldstein, H., Lei, L., Sonabend, A., Yun, J., Samanamud, J., Sims, J.S., Banu, M., et al. (2014). MRI-localized biopsies reveal subtype-specific differences in molecular and cellular composition at the margins of glioblastoma. Proc. Natl. Acad. Sci. USA *111*, 12550–12555.

Hanahan, D., and Folkman, J. (1996). Patterns and emerging mechanisms of the angiogenic switch during tumorigenesis. Cell *86*, 353–364.

Hu, J., Ho, A.L., Yuan, L., Hu, B., Hua, S., Hwang, S.S., Zhang, J., Hu, T., Zheng, H., Gan, B., et al. (2013). From the Cover: Neutralization of terminal differentiation in gliomagenesis. Proc. Natl. Acad. Sci. USA *110*, 14520–14527.

Jeong, H.M., Jin, Y.H., Kim, Y.J., Yum, J., Choi, Y.H., Yeo, C.Y., and Lee, K.Y. (2011). Akt phosphorylates and regulates the function of Dlx5. Biochem. Biophys. Res. Commun. *409*, 681–686.

Lathia, J.D., Heddleston, J.M., Venere, M., and Rich, J.N. (2011). Deadly teamwork: Neural cancer stem cells and the tumor microenvironment. Cell Stem Cell *8*, 482–485.

Liu, Q., Nguyen, D.H., Dong, Q., Shitaku, P., Chung, K., Liu, O.Y., Tso, J.L., Liu, J.Y., Konkankit, V., Cloughesy, T.F., et al. (2009). Molecular properties of CD133+ glioblastoma stem cells derived from treatment-refractory recurrent brain tumors. J. Neurooncol. *94*, 1–19.

Lobo, N.A., Shimono, Y., Qian, D., and Clarke, M.F. (2007). The biology of cancer stem cells. Annu. Rev. Cell Dev. Biol. *23*, 675–699.

Masckauchán, T.N., Agalliu, D., Vorontchikhina, M., Ahn, A., Parmalee, N.L., Li, C.M., Khoo, A., Tycko, B., Brown, A.M., and Kitajewski, J. (2006). Wnt5a signaling induces proliferation and survival of endothelial cells in vitro and expression of MMP-1 and Tie-2. Mol. Biol. Cell *17*, 5163–5172.

Mayes, D.A., Hu, Y., Teng, Y., Siegel, E., Wu, X., Panda, K., Tan, F., Yung, W.K., and Zhou, Y.H. (2006). PAX6 suppresses the invasiveness of glioblastoma cells and the expression of the matrix metalloproteinase-2 gene. Cancer Res. *66*, 9809–9817.

Molina, J.R., Hayashi, Y., Stephens, C., and Georgescu, M.M. (2010). Invasive glioblastoma cells acquire stemness and increased Akt activation. Neoplasia *12*, 453–463.

Paina, S., Garzotto, D., DeMarchis, S., Marino, M., Moiana, A., Conti, L., Cattaneo, E., Perera, M., Corte, G., Calautti, E., and Merlo, G.R. (2011). Wnt5a is a transcriptional target of Dlx homeogenes and promotes differentiation of interneuron progenitors in vitro and in vivo. J. Neurosci. *31*, 2675–2687.

Phillips, H.S., Kharbanda, S., Chen, R., Forrest, W.F., Soriano, R.H., Wu, T.D., Misra, A., Nigro, J.M., Colman, H., Soroceanu, L., et al. (2006). Molecular subclasses of high-grade glioma predict prognosis, delineate a pattern of disease progression, and resemble stages in neurogenesis. Cancer Cell *9*, 157–173.

Ricci-Vitiani, L., Pallini, R., Biffoni, M., Todaro, M., Invernici, G., Cenci, T., Maira, G., Parati, E.A., Stassi, G., Larocca, L.M., and De Maria, R. (2010). Tumour vascularization via endothelial differentiation of glioblastoma stem-like cells. Nature *468*, 824–828.

Rodriguez, F.J., Orr, B.A., Ligon, K.L., and Eberhart, C.G. (2012). Neoplastic cells are a rare component in human glioblastoma microvasculature. Oncotarget *3*, 98–106.

Shang, Y., Hu, X., DiRenzo, J., Lazar, M.A., and Brown, M. (2000). Cofactor dynamics and sufficiency in estrogen receptor-regulated transcription. Cell *103*, 843–852.

Shen, Q., Goderie, S.K., Jin, L., Karanth, N., Sun, Y., Abramova, N., Vincent, P., Pumiglia, K., and Temple, S. (2004). Endothelial cells stimulate self-renewal and expand neurogenesis of neural stem cells. Science *304*, 1338–1340.

Singh, S.K., Hawkins, C., Clarke, I.D., Squire, J.A., Bayani, J., Hide, T., Henkelman, R.M., Cusimano, M.D., and Dirks, P.B. (2004). Identification of human brain tumour initiating cells. Nature *432*, 396–401.

Soda, Y., Marumoto, T., Friedmann-Morvinski, D., Soda, M., Liu, F., Michiue, H., Pastorino, S., Yang, M., Hoffman, R.M., Kesari, S., and Verma, I.M. (2011). Transdifferentiation of glioblastoma cells into vascular endothelial cells. Proc. Natl. Acad. Sci. USA *108*, 4274–4280.

Sottoriva, A., Spiteri, I., Piccirillo, S.G., Touloumis, A., Collins, V.P., Marioni, J.C., Curtis, C., Watts, C., and Tavaré, S. (2013). Intratumor heterogeneity in human glioblastoma reflects cancer evolutionary dynamics. Proc. Natl. Acad. Sci. USA *110*, 4009–4014.

Subramanian, A., Tamayo, P., Mootha, V.K., Mukherjee, S., Ebert, B.L., Gillette, M.A., Paulovich, A., Pomeroy, S.L., Golub, T.R., Lander, E.S., and Mesirov, J.P. (2005). Gene set enrichment analysis: A knowledge-based approach for interpreting genome-wide expression profiles. Proc. Natl. Acad. Sci. USA *102*, 15545–15550.

Suzuki, Y., Shirai, K., Oka, K., Mobaraki, A., Yoshida, Y., Noda, S.E., Okamoto, M., Suzuki, Y., Itoh, J., Itoh, H., et al. (2010). Higher pAkt expression predicts a significant worse prognosis in glioblastomas. J. Radiat. Res. (Tokyo) *51*, 343–348.

Wang, H., Wang, H., Zhang, W., Huang, H.J., Liao, W.S., and Fuller, G.N. (2004). Analysis of the activation status of Akt, NFkappaB, and Stat3 in human diffuse gliomas. Lab. Invest. *84*, 941–951.

Wang, R., Chadalavada, K., Wilshire, J., Kowalik, U., Hovinga, K.E., Geber, A., Fligelman, B., Leversha, M., Brennan, C., and Tabar, V. (2010). Glioblastoma stem-like cells give rise to tumour endothelium. Nature *468*, 829–833.

Wen, P.Y., and Kesari, S. (2008). Malignant gliomas in adults. N. Engl. J. Med. *359*, 492–507.

Yang, D.H., Yoon, J.Y., Lee, S.H., Bryja, V., Andersson, E.R., Arenas, E., Kwon, Y.G., and Choi, K.Y. (2009). Wnt5a is required for endothelial differentiation of embryonic stem cells and vascularization via pathways involving both Wnt/beta-catenin and protein kinase Calpha. Circ. Res. *104*, 372–379.

Zhang, Y., Liu, T., Meyer, C.A., Eckhoute, J., Johnson, D.S., Bernstein, B.E., Nusbaum, C., Myers, R.M., Brown, M., Li, W., et al. (2008). Model-based analysis of ChIP-Seq (MACS). Genome Biol. *9*, R137.

Zheng, H., Ying, H., Yan, H., Kimmelman, A.C., Hiller, D.J., Chen, A.J., Perry, S.R., Tonon, G., Chu, G.C., Ding, Z., et al. (2008). p53 and Pten control neural and glioma stem/progenitor cell renewal and differentiation. Nature *455*, 1129–1133.

Zhou, Y.H., Wu, X., Tan, F., Shi, Y.X., Glass, T., Liu, T.J., Wathen, K., Hess, K.R., Gumin, J., Lang, F., and Yung, W.K. (2005). PAX6 suppresses growth of human glioblastoma cells. J. Neurooncol. *71*, 223–229.

Zhu, T.S., Costello, M.A., Talsma, C.E., Flack, C.G., Crowley, J.G., Hamm, L.L., He, X., Hervey-Jumper, S.L., Heth, J.A., Muraszko, K.M., et al. (2011). Endothelial cells create a stem cell niche in glioblastoma by providing NOTCH ligands that nurture self-renewal of cancer stem-like cells. Cancer Res. *71*, 6061–6072.

Zhu, Z., Khan, M.A., Weiler, M., Blaes, J., Jestaedt, L., Geibert, M., Zou, P., Gronych, J., Bernhardt, O., Korshunov, A., et al. (2014). Targeting self-renewal in high-grade brain tumors leads to loss of brain tumor stem cells and prolonged survival. Cell Stem Cell *15*, 185–198.

STAR★METHODS

KEY RESOURCES TABLE

REAGENT or RESOURCE	SOURCE	IDENTIFIER
Antibodies		
Rabbit polyclonal anti-AKT	Cell Signaling Technology	Cat# 9272 RRID:AB_329827
Rabbit polyclonal anti-Phospho-Akt (Ser473)	Cell Signaling Technology	Cat# 9271 RRID:AB_329825
Rabbit monoclonal anti-Phospho-Akt (Thr308) (244F9)	Cell Signaling Technology	Cat# 4056 RRID:AB_331163
Rabbit monoclonal anti-Phospho-S6 Ribosomal Protein (Ser235/236) (D57.2.2E) XP	Cell Signaling Technology	Cat# 4858S RRID:AB_916156
Mouse monoclonal anti-S6 Ribosomal Protein (54D2)	Cell Signaling Technology	Cat# 2317 RRID:AB_2238583
Rabbit monoclonal anti-Phospho-p70 S6 Kinase (Thr389) (108D2)	Cell Signaling Technology	Cat# 9234P RRID:AB_10121787
Rabbit monoclonal anti-p70 S6 Kinase	Cell Signaling Technology	Cat# 2708 RRID:AB_390722
Rabbit polyclonal anti-p44/42 MAPK (Erk1/2)	Cell Signaling Technology	Cat# 9102L RRID:AB_823494
Rabbit polyclonal anti-Phospho-p44/42 MAPK (Erk1/2) (Thr202/Tyr204)	Cell Signaling Technology	Cat# 9101 RRID:AB_331646
Rabbit monoclonal anti -Wnt5a/b (C27E8)	Cell Signaling Technology	Cat# 2530S RRID:AB_2215595
Rabbit monoclonal anti-VEGFR2 (55B11)	Cell Signaling Technology	Cat# 2479L RRID:AB_2212507
Rabbit polyclonal anti-Phospho-CaMKII (Thr286)	Cell Signaling Technology	Cat# 3361 RRID:AB_10015209
Rabbit polyclonal anti-CaMKII (pan)	Cell Signaling Technology	Cat# 3362 RRID:AB_2067938
Rabbit polyclonal anti-p53 (FL-393)	Santa Cruz Biotechnology	Cat# sc-6243 RRID:AB_653753
Goat polyclonal anti-DLX5 (ChIP)	Santa Cruz Biotechnology	Cat# sc-18152 RRID:AB_2090874
Mouse monoclonal anti-PAX6 (WB)	Santa Cruz Biotechnology	Cat# sc-81649 RRID:AB_1127044
Normal rabbit IgG antibody	Santa Cruz Biotechnology	Cat# sc-3888 RRID:AB_737196
Normal goat IgG antibody	Santa Cruz Biotechnology	Cat# sc-2028 RRID:AB_737167
CD31-APC, human (clone: AC128)	Miltenyi biotec	Cat#130-092-652
CD144 (VE-Cadherin)-FITC, human (clone: REA199)	Miltenyi biotec	Cat#130-100-742
CD144 (VE-Cadherin)-APC, human (clone: REA199)	Miltenyi biotec	Cat#130-100-708
CD133/1 (AC133)-PE, human (clone: AC133)	Miltenyi biotec	Cat#130-080-801
Mouse monoclonal anti-b-Actin (Clone AC-74)	Sigma-Aldrich	Cat# A2228
Rabbit polyclonal anti-PAX6(IHC)	Sigma-Aldrich	Cat# HPA030775 RRID:AB_10601243
Rabbit polyclonal anti-DLX5(WB/IHC)	Sigma-Aldrich	Cat# HPA005670 RRID:AB_1078681
Mouse monoclonal anti-CD105 (Endoglin, SN6h)	DAKO	Cat# M3527 RRID:AB_2099044
Rabbit polyclonal anti-Glial Fibrillary Acidic Protein (GFAP)	DAKO	Cat# N1506 RRID:AB_10013482
Rabbit monoclonal anti-Ki67	Vector Laboratories	Cat# VP-RM04 RRID:AB_2336545
Rabbit polyclonal anti-VEGF Receptor 2	Abcam	Cat# ab39256 RRID:AB_883437
Rabbit polyclonal anti-Von Willebrand Factor	Abcam	Cat# ab9378 RRID:AB_307223
Rabbit polyclonal anti-CD31	Abcam	Cat# ab28364 RRID:AB_726362
Mouse monoclonal anti-CD31	Abcam	Cat# ab9498 RRID:AB_307284
Rabbit polyclonal anti-H3K27ac	Abcam	Cat# ab4729 RRID:AB_2118291

(*Continued on next page*)

Continued

REAGENT or RESOURCE	SOURCE	IDENTIFIER
Rabbit polyclonal anti-H3K4me1	Abcam	Cat# ab8895, RRID:AB_306847
Rabbit polyclonal anti-PAX6 (ChIP)	Abcam	Cat# ab5790 RRID:AB_305110
Rabbit monoclonal anti-SOX2 (EPR3131)	Abcam	Cat# ab92494 RRID:AB_10585428
Mouse monoclonal anti-Nestin (10C2)	Abcam	Cat# ab22035 RRID:AB_446723
Rabbit polyclonal anti-Histone H3K4me2	Active Motif	Cat# 39141 RRID: AB_2614985
Rabbit polyclonal anti-H3K27me3	EMD Millipore	Cat# 07-449 RRID:AB_310624
Rabbit polyclonal anti-H3K4me3	EMD Millipore	Cat# 07-473 RRID:AB_1977252
Rabbit monoclonal anti-CD34 (EP373Y)	GeneTex	Cat# GTX61737 RRID:AB_10624965
Mouse monoclonal anti-Human TRA-1-85	R&D Systems	Cat# MAB3195 RRID:AB_2066681
Rabbit monoclonal anti-Neuronal Class III beta-Tubulin (TUJ1)	Covance Research	Cat# MRB-435P-100 RRID:AB_10175616
Mouse monoclonal anti-CD144	BD Biosciences	Cat# 555661 RRID:AB_396015
Mouse monoclonal anti-eNOS/NOS Type III	BD Biosciences	Cat# 610297 RRID:AB_397691
Chemicals, Peptides, and Recombinant Proteins		
Wnt Antagonist III, Box5	Calbiochem	Cat# 681673
Wnt-5a Recombinant Protein	R&D Systems	Cat# 645-WN
Wnt-3a Recombinant Protein	R&D Systems	Cat# 5036-WN
Ganciclovir (GCV)	InvivoGen	CAS # 82410-32-0 Cat. Code sud-gcv
Iodonitrotetrazolium chloride	Sigma-Aldrich	Cat# I10406
Calcein AM	BD Biosciences	Cat#564061
Critical Commercial Assays		
DiI-AcLDL Uptake Assay	Thermo Fisher	Cat# L35353
NEBNext DNA Library Prep kit	New England BioLabs	Cat# E7370S
BD FluoroBlok System	BD Biosciences	Cat# BD351161
TumorTACS In Situ Apoptosis Detection Kit	Trevigene	Cat# 4815-30-K
MACH 2 Double Stain 1	Biocare Medical	Cat# MRCT523G
MACH 2 Double Stain 2	Biocare Medical	Cat# MRCT525G
Deposited Data		
Gene expression profile	NCBI Gene Expression Omnibus	GEO:GSE85615
ChIP sequencing data	NCBI Gene Expression Omnibus	GEO: GSE86624
Experimental Models: Cell Lines		
Myc-immortalized human neural progenitor cells (ReNcell)	EMD Millipore	Cat# SC007
Myc-immortalized human neural stem cells	This paper	N/A
Patient derived GSC lines (TS543, TS576,TS586,TS603)	Laboratory of Dr. Cameron W. Brennan (MSKCC)	N/A
Patient derived GSC lines (BT112,BT147)	Laboratory of Dr. Keith L. Ligon (DFCI)	N/A
293T packaging cells	ATCC	CRL-11268
Human umbilical vein endothelial cells (HUVEC)	ScienCell Research Laboratories	Cat#8000
Human Brain Microvascular Endothelial Cells (HBMECs)	ScienCell Research Laboratories	Cat#1000
Human Brain Microvascular Endothelial Cells (HBMECs)	Neuromics	Cat# HEC02
Experimental Models: Organisms/Strains		
Mouse: ICR SCID female	Taconic	ICRSC-F
Recombinant DNA		
pWZL-Blast-myc	Addgene	Cat#10674
pCMVR8.74	Addgene	Cat#22036

(*Continued on next page*)

Continued

REAGENT or RESOURCE	SOURCE	IDENTIFIER
pMD2.G	Addgene	Cat#12259
pLenti6.3/V5-DEST gateway Vector	Thermo Fisher	Cat#V53306
pLVX-ZsGreen1-N1	Clontech	Cat#632565
cEF.tk-GFP	Addgene	Cat#33308
pLenti6.3-GFP	This paper	N/A
pWZ-neo-myr-AKT	This paper	N/A
pLenti6.3-myr-AKT	This paper	N/A
pLenti6.3-p53DN	This paper	N/A
pLenti6.3-CXCL14	This paper	N/A
pLenti6.3-DLX5	This paper	N/A
pLenti6.3-DMRT3	This paper	N/A
pLenti6.3-GPR37	This paper	N/A
pLenti6.3-MYLIP	This paper	N/A
pLenti6.3-NUDT14	This paper	N/A
pLenti6.3-TCF7	This paper	N/A
pLenti6.3-WNT5A	This paper	N/A
pLenti6.3-PAX6	This paper	N/A
pCD144-HSVTK-GFP	This paper	N/A
pLKO.1 target gene set (CXCL14)	Sigma-Aldrich	SHCLNG-NM_004887
pLKO.1 target gene set (DLX5)	Sigma-Aldrich	SHCLNG-NM_005221
pLKO.1 target gene set (DMRT3)	Sigma-Aldrich	SHCLNG-NM_021240
pLKO.1 target gene set (GPR37)	Sigma-Aldrich	SHCLNG-NM_005302
pLKO.1 target gene set (MYLIP)	Sigma-Aldrich	SHCLNG-NM_013262
pLKO.1 target gene set (NUDT14)	Sigma-Aldrich	SHCLNG-NM_177533
pLKO.1 target gene set (TCF7)	Sigma-Aldrich	SHCLNG-NM_003202
pLKO.1 target gene set (WNT5A)	Sigma-Aldrich	SHCLNG-NM_003392
Sequence-Based Reagents		
All primers and oligonucleotides are listed in Table S7	This paper	N/A
Software and Algorithms		
InForm Cell Analysis Version 2.2	PerkinElmer	http://www.perkinelmer.com/lab-products-and-services/resources/software-downloads.html#inForm
Flow Jo_v10	FlowJo	http://www.flowjo.com/
Pannoramic Viewer	3DHISTECH Ltd.	http://www.3dhistech.com/pannoramic_viewer
ImageJ	National Institutes of Health	https://imagej.nih.gov/ij/
Aperio ImageScope_v12	Leica Biosystems	http://www.leicabiosystems.com/digital-pathology/digital-pathology-management/imagescope/
Integrative Genomics Viewer (IGV)	The Broad Institute of MIT and Harvard	http://software.broadinstitute.org/software/igv/
R package (Version 3.2.5)	The R Project for Statistical Computing	https://www.r-project.org
Model-based Analysis of ChIP-Seq (MACS)	Zhang et al., 2008	https://genomebiology.biomedcentral.com/articles/10.1186/gb-2008-9-9-r137
Data Visualization Tools for Brain Tumor Datasets	N/A	http://gliovis.bioinfo.cnio.es

CONTACT FOR REAGENT AND RESOURCE SHARING

Further information and requests for reagents may be directed to, and will be fulfilled by the corresponding author Ronald A. DePinho (rdepinho@mdanderson.org).

EXPERIMENTAL MODEL AND SUBJECT DETAILS

Cell Lines and Cell Culture

The c-*myc*-immortalized human neural progenitor cells (ReNcell) were purchased from Millipore (EMD Millipore, Billerica, MA). Another human neural stem cell line (NSC) was derived from 18-week gestation fetal brain tissue that was provided by Dr. Volney L. Sheen (BIDMC, Harvard Medical School, Boston, MA, USA), which was immortalized by c-MYC (pWZL-Blast-MYC, Addgene). Patient-derived glioma stem cells (GSCs) were provided by Dr. Cameron W. Brennan (Memorial Sloan Kettering Cancer Center, New York, NY, USA) and by Dr. Keith L. Ligon (Dana-Farber Cancer Institute, Boston, MA, USA). All NSCs and GSCs were cultured in NSC proliferation media (Millipore Corporation, Billerica, MA) with 20 ng/ml EGF and 20 ng/ml bFGF. Human umbilical vein endothelial cells (HUVECs) and human brain microvascular endothelial cells (HBMECs) were purchased from ScienCell and Neuromics and were cultured in endothelial cell media (ECM, Cat#1001, ScienCell; MED001, Neuromics).The 293T packaging cells from ATCC were cultured in DMEM with 10% FBS.

Mice and Animal Housing

Female ICR SCID mice at 3-4 weeks age were purchased from Taconic Biosciences. Mice were grouped by 5 animals in large plastic cages and were maintained under pathogen-free conditions. All animal experiments were performed with the approval of MD Anderson Cancer Center's Institutional Animal Care and Use Committee (IACUC).

Intracranial Xenograft Tumor Models

Female SCID mice were anesthetized and placed into stereotactic apparatus equipped with a z axis (Stoelting). A small hole was bored in the skull 0.5 mm anterior and 3.0 mm lateral to the bregma using a dental drill. Cells (2×10^5 in Figure 1C; 200-200,000 in Figure S1C) in 5 μl Hanks Balanced Salt Solution were injected into the right caudate nucleus 3 mm below the surface of the brain using a 10 μL Hamilton syringe with an unbeveled 30-gauge needle. Alternatively, mice were bolted before the intracranial implantation at MD Anderson's Brain Tumor Center Animal Core. To install guide screw, animals were anesthetized by intraperitoneal injection with ketamine/xylazine solution (200 mg ketamine and 20 mg xylazine in 17 mL of saline) at a dosage of 0.15 mg/10 g body weight. The plastic screw was rotated into a small drill hole made 2.5 mm lateral and 1 mm anterior to the bregma and the central hole of the guide screw was closed by placing a cross-shaped stylet inside it. After one week recovery, mice were grouped by four or five animal for cells implantation. The cells (5×10^5 in Figure S5D; 1×10^4 in Figure S5M) were injected in 5 μl Hanks Balanced Salt Solution. Animals were followed daily for the development of tumors. Mice with neurological deficits or moribund appearance were sacrificed. Brains were removed using transcardial perfusion with 4% paraformaldehyde (PFA) and were fixed in formalin or post-fixed in 4% PFA and processed for paraffin embedded or OCT frozen tissue blocks.

METHOD DETAILS

Lentivirus Production and Transduction of Target Cells

The expression vectors (p53 dominant negative-p53DN, myr-AKT, CXCL14, DLX5, DMRT3, GPR37, MYLIP, NUDT14, TCF7, WNT5A, and PAX6) were generated by cloning the respective open reading frame (ORF) into pLenti6.3 vector using Gateway Cloning system. The pLKO.1 shRNAs were purchased from Sigma. Gene expression was validated by qRT-PCR or immunoblotting in lentivirus infected target cells. Lentiviruses were produced in 293T cells with packaging system (pCMVR8.74, pMD2.G, Addgene) as per Vendor's instruction.

Immunoblotting (IB), Immunohistochemistry (IHC) and Immunofluorescence (IF)

For immunoblotting, cells were harvested, washed with phosphate buffered saline, lysed in RIPA buffer (150 mM NaCl, 50 mM Tris [pH 8.0], 1.0% Igepal CA-630, 0.5% sodium deoxycholate, 0.1% sodium dodecyl sulfate [SDS]; Sigma) with protease inhibitor cocktail tablet complete mini (Roche Diagnostics), phosphatase inhibitor cocktail 2 (Sigma) and 1 μM DTT, and centrifuged at 10,000 × g at 4°C for 15 min. Protein lysates were subjected to SDS-polyacrylamide gel electrophoresis on 4%–12% gradient polyacrylamide gel (NuPage, Thermo Fischer Scientific), transferred onto nitrocellulose membranes which were incubated with indicated primary antibodies, washed, and probed with HRP-conjugated secondary antibodies. For IHC staining, brain sections were incubated with indicated primary antibodies for 1 hr at room temperature (RT) or overnight at 4°C after deparaffinization, rehydration, antigen retrieval, quenching of endogenous peroxidase and blocking. The sections were incubated with horseradish peroxidase (HRP)-conjugated polymer (DAKO) for 40 min and then Diaminobenzidine using Ultravision DAB Plus Substrate Detection System (Thermo Fischer Scientific) for 1-10 min at RT, followed by hematoxylin staining. For IF staining, OCT frozen brain sections were thawed at RT for 30 min, rinsed and rehydrated with phosphate buffered saline 3 times. After blocking with PBS buffer containing 10% FBS,

1% BSA and 0.3% Triton, the sections were incubated with indicated primary antibodies overnight at 4°C. The samples were then incubated with species-appropriate donkey secondary antibodies coupled to AlexaFluor dyes (488, 555, 568 or 594, 647, Invitrogen) for 1 hr at RT. VECTASHIELD with DAPI (Vector Laboratories) was used to mount coverslips. The slides were scanned using the digital slide scanner, Pannoramic 250 Flash II (3DHISTECH, Ltd.) and images analyzed by Pannoramic viewer.

Flow Cytometry and FACS Sorting

Cells were harvested and suspended in ice-cold PBS with 1% BSA and 2mM EDTA. After incubation with FcR Blocking Reagent (Miltenyi Biotec), cells were stained by fluorescently conjugated antibodies and incubated for 10 min in the dark in the refrigerator (2−8°C). Antibodies include CD31-APC, CD144-FITC, CD144-APC, CD133-PE, IgG-APC, IgG-FITC, and IgG-PE from Miltenyi Biotec. The stained cells or GFP-labeled cells were analyzed in a BD Fortessa analyzer. FACS sorting was performed using the BD FACSAria cell sorter. Data were analyzed using FlowJo software.

Chromatin Immunoprecipitation Sequencing (ChIP-Seq) and ChIP-qPCR

Chromatin Immunoprecipitation (ChIP) was performed on early passage cell lines, hNSCs and three tumor neurosphere lines derived from hNSC transduced with p53DN and myr-AKT as previously described (Shang et al., 2000). Briefly, cells (~2×10^6 cells per ChIP) were cross-linked in 1% formaldehyde solution, re-suspended, and lysed. Cell lysates were solubilized, and cross-linked chromatin was sheared to a size range of 100 to 300 bases using a Bioruptor Sonicator (Diagenode, UCD-200). Solubilized chromatin was diluted 10-fold in ChIP dilution buffer and incubated at 4°C with 2 μg antibodies against specific histone modification or transcription factors. The following antibodies were used in ChIP assays: anti-H3K27me3, anti-H3K27ac, anti-H3K4me3, anti-H3K4me1, anti-H3K4me, anti-PAX6, anti-DLX5, normal rabbit IgG and normal goat IgG. After ChIP, samples were washed, and bound complexes were eluted and reverse cross-linked. Multiplexed and barcoded sequencing libraries for ChIPed DNA and Input DNA were generated with NEBNext Library Prep kit according to the manufacturer's instructions, and then were sequenced by Illumina HiSeq 2000. Histone modification peaks and transcription factor-bound regions were identified as genomic regions with a significant read enrichment in ChIPed reads over the Input reads analyzed by the Model-based Analysis of ChIP-Seq (MACS) tool (Zhang et al., 2008). For ChIP-qPCR assays, the fold enrichment of ChIPed DNA relative to input DNA at a given genomic site was determined by comparative CT (ΔΔ CT) method using Power SYBR Green PCR Master Mix (Applied Biosystems) according to the manufacturer's protocol. An 18S rRNA genomic region was used for normalization. The primers used for ChIP-qPCR are listed in Table S7.

RNA Isolation, qRT-PCR and DNA Microarray

RNA was isolated with RNeasy Mini Kit (QIAGEN), and then used for first-strand cDNA synthesis using random primers and SuperScriptIII Reverse Transcriptase (Invitrogen). qRT–PCR was performed using Power SYBR Green PCR Master Mix (Applied Biosystems). Primers are listed in Table S7. The relative expression of genes was normalized using ribosomal protein L39 (RPL39) as a housekeeping gene.

Early passage cell lines, including hNSC, hNSC-p53DN, two independent lines for hNSC-P53DN-AKT, three tumor neurosphere lines derived from hNSC-P53DN-AKT (iGSC-1, iGSC-2, and iGSC-3), and FACS-sorting cells were grown in NSC proliferation media with EGF and bFGF for 24 hr. RNA was isolated using Trizol (Invitrogen) and the RNeasy mini kit (QIAGEN). Gene expression profiling was performed using the Affymetrix U133 Plus 2.0 Array at DFCI and MD Anderson's Sequencing and Microarray core facility.

Anchorage-Independent Growth Assays, Transwell Assay and Matrigel-based Tube Formation Assay

Anchorage-independent growth assays were performed in triplicate in 6-well plates or in 48-well plates. Indicated cells (2×10^4 or 1×10^3 per well) were seeded in NSC proliferation media with EGF and bFGF containing 0.4% low-melting agarose on the top of bottom agar containing 1% low-melting agarose NSC proliferation media with EGF and FGF. After 14 – 21 days, colonies were stained with Iodonitrotetrazolium chloride (Sigma) and counted.

Transwell assays were performed in BD FluoroBlok 96-multiwell insert systems (3.0 μm pore sizes) as per manufacturer's protocol (BD biosciences). HBMECs were seeded in transwell inserts at 1×10^4 cells/ well in EC media overnight. After 4 hr starvation in EC basal media at 37°C, 5% CO_2 incubator, the inserts were transferred into the basal chambers containing chemoattractant in NSC media as indicated. After 24 hr incubation, the inserts were transferred into a second 96-well plate containing 4 μg/mL Calcein AM (BD biosciences) in DPBS. Incubate for 1 hr at 37°C, 5% CO_2, fluorescence of invaded cells was read at wavelengths of 494/517 nm (Ex/Em) on fluorescent plate reader. Neurosphere formation was performed by transwell assay in 24-well plate by culturing sorted GdECs or non-GdECs with HBMECs (1×10^4 of indicated cells) in transwell inserts containing NSC media, and GSC being cultured in basal chamber at 1 cell per microliter (500 μl/well) in NSC media. GSC neurospheres were counted after 7 days.

EC tubular formation was assessed by growth factor reduced Matrigel assay kit (BD Biosciences) in three-dimensional (3D) culture according to the manufacturer's instructions. The $CD133^+/CD144^+$ cells sorted from p53DN-AKT-hNSCs were infected by lentivirus carrying shRNA targeting the indicated genes (Figures 3C and 3D) or were treated with BOX5 (100μM) (Figures 3F and 3G). Cells were harvested at 48 hr post-infection or treatment and then were cultured in growth factor reduced Matrigel. Quantification was performed after 8-12 hr. To quantify the tubular formation, branch points (3 or more tubular branches emanating from a point) were analyzed with an inverted microscope at 40x magnification and counted in 5 random fields per well.

Magnetic Resonance Imaging (MRI)

MRI studies were performed on the 4.7 T Biospec USR MRI system (Bruker Biospin MRI, Billerica, MA) in MD Anderson's Small Animal Cancer Imaging Research Facility. Animals were anesthetized with 1.5%–5% isoflurane inhalation anesthesia. Images of brains were acquired using T2-weighted axial and coronal Rapid Acquisition with Relaxation Enhancement (RARE) scans with TR = 3000 ms, TE = 57 ms, RARE factor = 12, 4 Averages, 156 μm in-plane resolution, 4 cm x 3 cm FOV, 0.75 mm slice thickness and 0.25 mm slice gap. Tumor volume was measured by contouring the lesions in the T2-weighted images using ImageJ software (National Institutes of Health, Bethesda, MD, USA). The total tumor volume is the sum of the in-plane tumor volumes and the sum of the tumor volumes within the slice gaps, which was estimated by multiplying the mean of the contoured areas on adjacent slices by the width of the slice gap.

Selective Targeting of GdECs in GBM xenografts by GCV/HSVTK system

To generate the plasmid of CD144 (VE-Cadherin)-promoter-driven expression of HSVTK plus GFP, the original promoter in pLVX-ZsGreen1-N1 (Clontech) was replaced by a PCR amplified 1.5 kb genomic region of human CD144 promoter. The fragment coding HSVTK-GFP amplified from cEF.tk-GFP (Addgene) by PCR was inserted into pLVX-ZsGreen1-N1 downstream of CD144 promoter to generate *p*CD144-HSVTK-GFP, in which the region of ZsGreen was removed and subsequently validated by sequencing. GSCs were transduced with *p*CD144-HSVTK-GFP though lentiviral infection and then transplanted into brains of SCID mice. Tumor-bearing animals were administrated GCV (InvoGen) at 80mg/kg/day or PBS daily through intraperitoneal injection. The xenograft tumors were collected for IHC and IF analyses. To detect GCV-induced apoptosis in GdECs expressing HSVTK, TUNEL assay was performed according to manufacturer's instructions (Trevigene).

Identification of Histone H3K27 Status Switch Genes and AKT Activation Signature Genes

Genomic regions within 2 kilobases upstream and downstream of gene transcriptional start sites (TSSs) were examined for histone modification peaks based on Model-based Analysis of ChIP-Seq (MACS). Histone H3K27 status switch genes were identified as a group of genes with dynamic histone modification changes of H3K27me3 and H3K27ac in iGSCs compared with hNSCs. AKT activation signature genes (417) were identified based on gene expression profile comparison: at least 2-fold changes for 3 independent tumor spheres lines derived from p53DN-AKT-hNSCs (iGSC-1, iGSC-2, and iGSC-3) versus hNSCs; two independent cell lines for p53DN-AKT-hNSCs (different levels of AKT activation) versus hNSCs; one line for p53DN-AKT-hNSCs (higher AKT levels) versus the other line for p53DN-AKT-hNSCs (lower AKT levels).

Clinical Datasets and Pathological Analysis

TCGA GBM datasets include gene mutations, copy number, gene expression, proteomics (RPPA), tumor subtypes and patient survival information (https://tcga-data.nci.nih.gov). Preprocessed gene expression profile and annotation of TCGA GBM samples were obtained from GlioVis. For the published datasets of human GBMs used in this study, gene expression profiles data for 9 pairs of intratumor and peritumor regions from GBM patients were obtained from ArrayExpress Archive (accession nos. E-MTAB-1215 and E-MTAB-1129)(Sottoriva et al., 2013); each gene mRNA expression was normalized to NES in Figures 7H and S7G. RNA-Seq data for 39 samples from contrast-enhancing (CE) regions and 36 samples from non-enhancing (NE) regions from 27 different glioma patients were obtained from Gene Expression Ominbus (accession number GSE59612) (Gill et al., 2014); each gene mRNA expression was normalized to NES in Figures S7H and S7I.

RNA-Seq data for 124 (81 pairs with IDHwt and pairwise profiles on the same platform for analysis in this study) paired primary and recurrent gliomas including both TCGA and in-house datasets were provided by Dr. Roel Verhaak's lab (MD Anderson). Frozen GBM tissues (n = 12) were obtained from TCGA collections and 10 primary GBMs (FFPE) blocks were obtained from Dr. Erik Sulman's lab. The paired primary/recurrent GBM slides (FFPE) for IHC were provided by the first Affiliated Hospital of Nanjing Medical University, Nanjing, China and Guangdong 999 Brain Hospital, Guangzhou, China. The pathological analysis of human GBMs was guided by board-certified neuropathologists. Aperio ImageScope and InForm software were used for identification and quantification. All human GBM tissue samples were analyzed with IRB-approval protocol (PA16-0408).

QUANTIFICATION AND STATISTICAL ANALYSIS

For quantification of microvessel density (MVD), images of tumor sections with IF or IHC staining were captured by using the digital slide scanner, Pannoramic 250 Flash II. Measurement was performed in a single area of intratumoral or peritumoral tumor (~0.178 mm^2 in Pannoramic view) representative of the highest microvessel density ("hot spot"). The CD34 positive cells or microvessels were counted. Five fields in each tumor were randomly selected for MVD analysis and statistical analysis was performed by using Welch's t test of Graphpad Prism6.

Quantification of GdECs by co-localization analysis using Caliper Vectra Image System and InForm software. Briefly, the IF or IHC (double staining-Wrap red and DAB) stained slides were loaded onto the Vectra slide scanner. Vectra Nuance 3.0.0 software was used to build the spectral libraries using 1 single chromogen only (e.g., DAPI, AlexaFluor-488, AlexaFluor-594, DAB, Wrap red, hematoxylin). Nuance multispectral image cubes were acquired with 20 × objective lens (0.5 micron/pixel) and using a full CCD frame at 1 × 1 binning (1360 × 1024 pixels) for analysis. For GdECs in IF stained xenograft tumors (Figure 5D), at least 3 image fields from 3

tumors with intratumoral and peritumoral areas were used for automated co-localization analysis using InForm software. Statistical analysis was performed by using unpaired Student's t test. For GdECs in IHC stained human GBM tumors sections (Figure 7K), 150 random images fields from 5 primary or recurrent GBM tumors were used for automated co-localization analysis using InForm software. Statistical analysis was performed by using Wilcoxon rank test.

To quantify cell distance in xenograft tumor sections (Figure 6B), the IF stained images were captured using the digital slide scanner, Pannoramic 250 Flash II and cell distance was measured manually using Pannoramic viewer. GdECs (GFP^+) were first located in the peritumoral regions (low cell density) and then the nearest host EC ($CD34^+/TRA\text{-}1\text{-}85^-$) within ~30μm of each respective GdEC was defined. The nearest tumor cells ($TRA\text{-}1\text{-}85^+/GFP^-$) to the defined host EC was then located. At least 5 fields in peritumoral areas for each tumor (n = 3) were selected for distance measurements. Statistical analysis was performed by using Welch's t test of Graphpad Prism6. To quantify cell distance in human GBM specimens (Figure 7C), 300 image fields from 10 human GBM tumors with IHC (double staining-Wrap red and DAB) staining were captured using Caliper Vectra Image System and analyzed data were generated using InForm software. GdECs were first located and the nearest host EC within 40 pixels (~28μm) of each respective GdEC was defined. The nearest GSC ($SOX2^+/CD31^-$) to the defined host EC ($SOX2^-/CD31^+$) was then located for calculation by using R package. Statistical analysis was performed by using Wilcoxon rank test.

To test the significance of overlap between stem cell pathways/genesets that compiled from MsigDB v5.1 and 85 genes with H3K27 acetylation (epigenetic activation), hypergeometric test was performed by using R package. P value for significance was given by 1-phyper (X, M, N, 85), where X is the size of overlapped genes, M is the number of genes in the stem cell related pathways for testing, and N is the number of genes that do not in stem cell related pathways. Based on this formula, the pathway of HEMATOPOIESIS_STEM_CELL NUMBER_LARGE_VS_TINY_UP was not significantly enriched (*p value* of hypergeometric test of overlap > 0.14), however, EC signaling pathway was significantly enriched (*p value* of hypergeometric test of overlap < 0.05) in these 85 genes (Figure 1)

Statistical information including *n*, mean and statistical significance values are indicated in the text or the figure legends. Animal survivals were analyzed using Log-rank test and cell distance and MVD were analyzed using Welch's t test based on Graphpad Prism6. Comparisons of cell growth, colony formation in anchorage-independent growth assays, tubular formation, transwell assay, neurosphere formation, and gene expression by qRT-PCR were performed using the unpaired Student's t test. Error bars in the experiments represent standard deviation (SD) of the mean values from either independent experiments or independent samples. All other statistical analyses were performed using R package (Version 3.2.5), and the detailed information about statistical methods were specified in figures/tables.

DATA AND SOFTWARE AVAILABILITY

Data Resources

The gene expression profile by microarray and the histone landscape by ChIP-Seq in this paper have been deposited in NCBI GEO: GSE85615 and GSE86624.

Cell

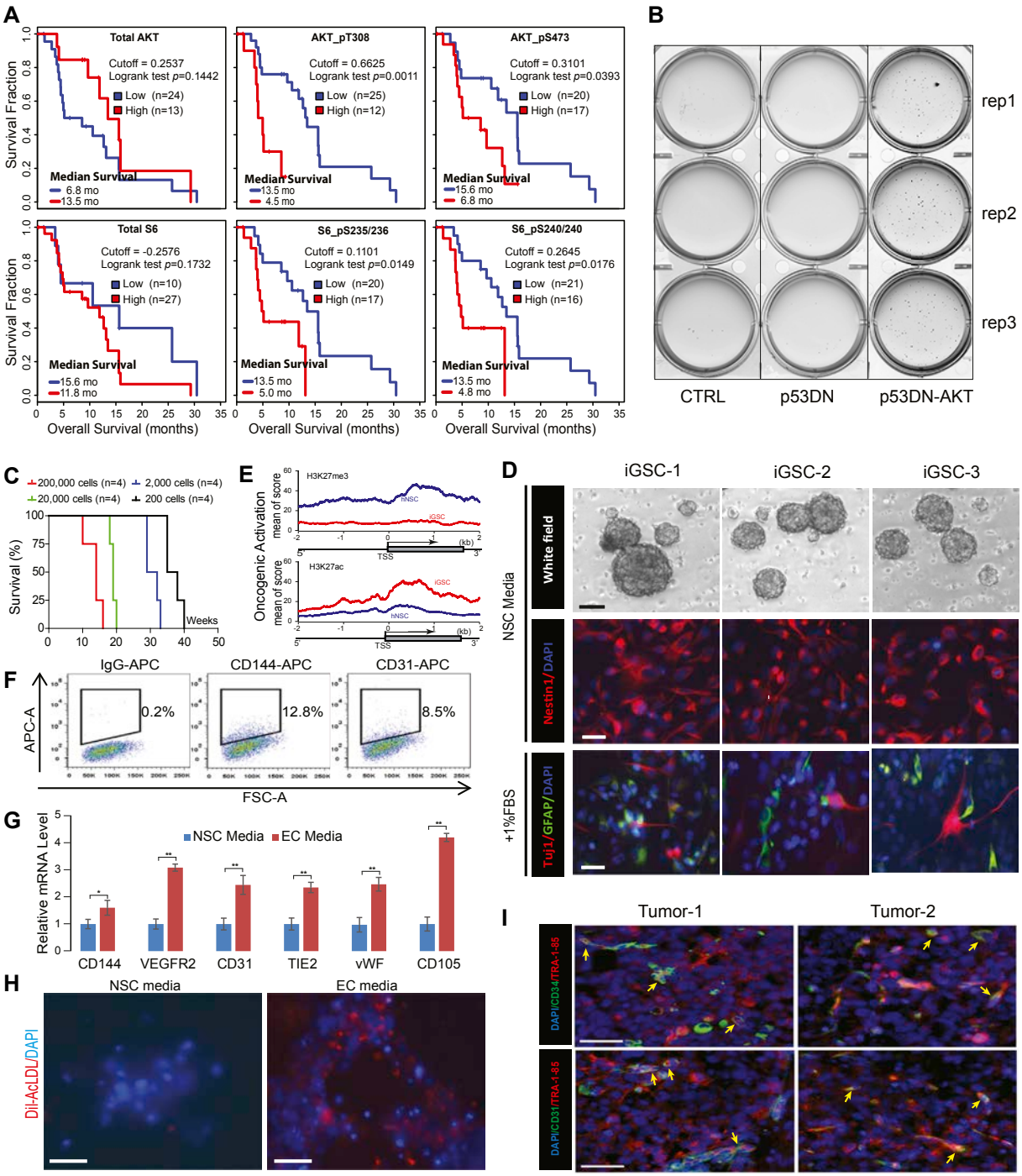

Figure S1. Characterization of EC Phenotypes in Tumor Neurospheres Derived from p53DN-AKT-hNSCs, Related to Figure 1

(A) Overall survival relative to the levels of AKT pathway activation in TCGA GBM cohorts. TCGA GBM samples with IDH wild-type, TP53 mutations, proteomic datasets (RPPA) and clinical data were divided into two groups according to the indicated protein levels by optimal cutoff. Patient survival relative to the levels of total AKT, AKT-pT308, AKT-pS473, S6, S6-pS235/236, and S6-pS240/244.

(B) Images for soft agar colony formation assay in 6-well plates showing transformation of hNSCs expressing p53DN, p53DN, and myr-AKT (p53DN-AKT).

(legend continued on next page)

(C) Tumor neurospheres (e.g., iGSC-1, iGSC-2, and iGSC-3) were isolated for secondary implant into mouse brain. Kaplan–Meier survival analysis after intracranial injection of different cell numbers of iGSC-2.
(D) Tumor cells were isolated from mouse brains and characterized by neurosphere formation and differentiation in vitro. Scale bars, 100 μm (black) and 50 μm (white).
(E) Mean of H3K27me3 and H3K27ac ChIP-Seq scores within 2 kb upstream and downstream of TSSs for 85 genes with H3K27 residue switch between hNSC and iGSC for oncogenic activation.
(F) Representative FACS analysis of the iGSCs expressing EC markers by CD144 and CD31 APC conjugated antibodies. FSC, forward scatter.
(G) qRT-PCR analysis of indicated EC marker expression in iGSCs under EC culture condition compared with NSC culture condition after 5 days. Error bars represent SD of the mean.*$p < 0.05$ and **$p < 0.01$.
(H) Representative images showing DiI-AcLDL uptake using iGSCs on matrigel supplemented with either EC media or NSC media. Scale bars, 50 μm.
(I) Representative images showing GdECs (yellow arrows) in tumor sections derived from p53DN-AKT-hNSCs by IF staining using the indicated markers. Scale bars, 40 μm.

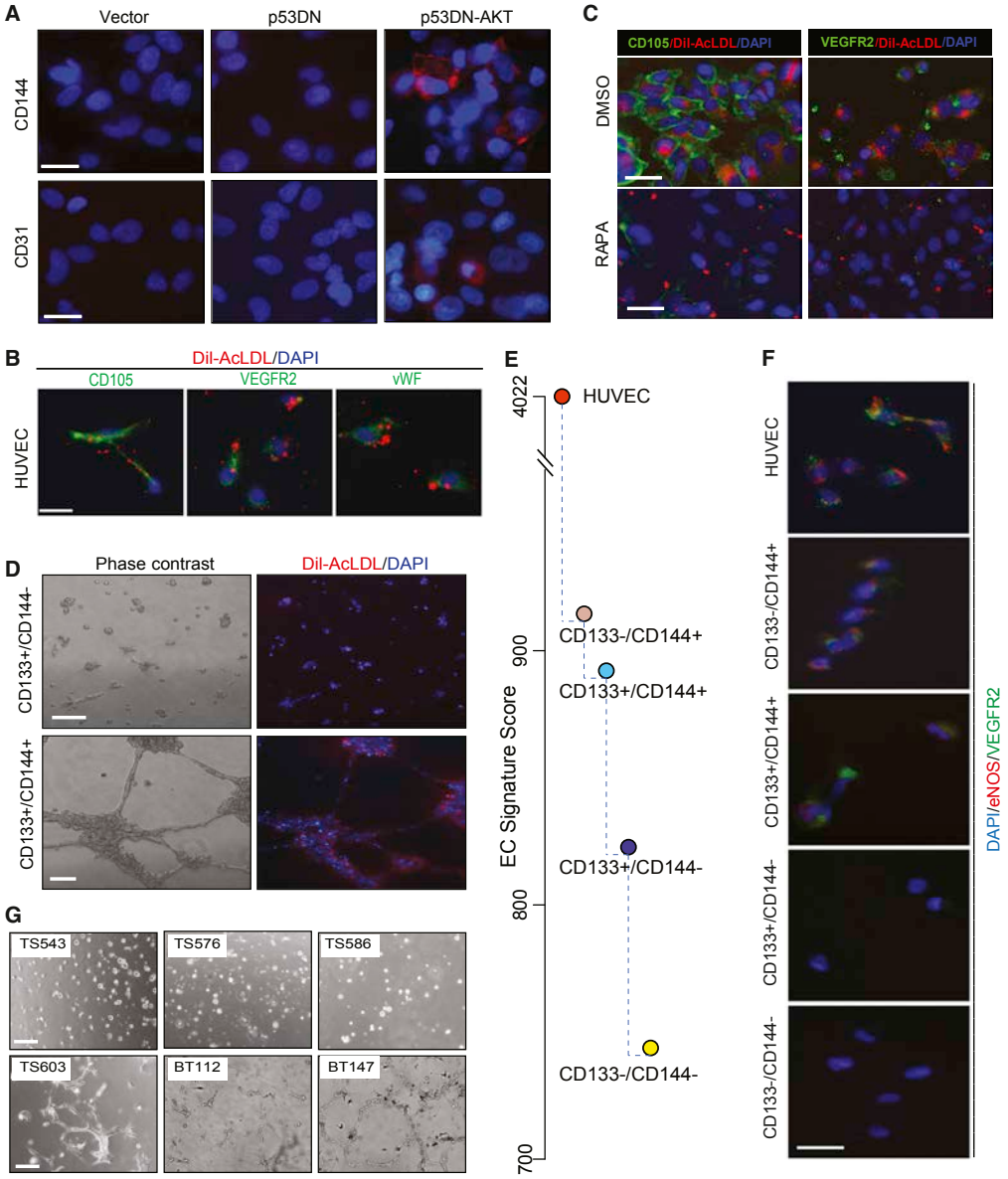

Figure S2. AKT Activation Induces Endothelial Lineage Differentiation of hNSCs, Related to Figure 2

(A) IF staining of CD144 and CD31 in hNSCs expressing empty vector (Vector), p53DN transduced hNSCs (p53DN) and p53DN-AKT transduced hNSCs (p53DN-AKT), Scale bars, 50 μm.

(B) Immunofluorescence analysis of HUVECs cultured with EC media for EC marker (CD105, VEGFR2, and vWF) expression and functional uptake of DiI-AcLDL. Scale bar, 40 μm.

(C) IF staining of EC marker (CD105 and VEGFR2) expression and DiI-AcLDL uptake with Rapamycin (RAPA) treatment (50 nM) in sorted $CD133^+/CD144^+$ cells from p53DN-AKT-hNSCs. Scale bars, 50 μm.

(D) Representative images showing tubular network formation and DiI-AcLDL uptake of sorted $CD133^+/CD144^+$ cells from p53DN-AKT-hNSCs under EC culture conditions. Scale bars, 100 μm (top) and 50 μm (bottom).

(E) EC signature scores were calculated using the gene expression profiles of HUVEC (GSE20986) and the p53DN-AKT-hNSCs sorted cell fractions, $CD133^-/CD144^-$, $CD133^+/CD144^-$, $CD133^+/CD144^+$, and $CD133^-/CD144^+$.

(F) Immunofluorescence analysis of sorted subpopulations from p53DN-AKT-hNSCs cultured with EC media for 3 days for EC marker (VEGFR2 and eNOS) expression. Scale bar, 40 μm.

(G) Representative images showing the formation of the tubular network on matrigel of patient-derived GSCs (TS543, TS576, TS586, TS603, BT112 and BT147) under EC culture conditions. Scale bars, 100 μm.

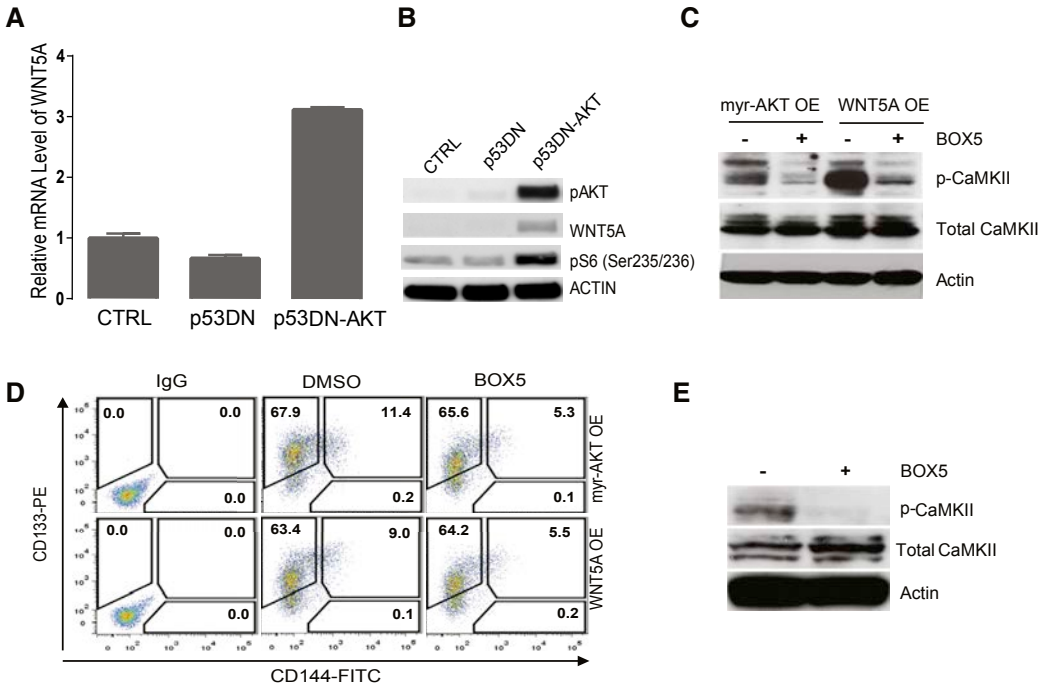

Figure S3. AKT Upregulates WNT5A in EC Lineage Differentiation of hNSCs, Related to Figure 3

(A) qRT-PCR and (B) Immunoblotting analyses of WNT5A expression in hNSCs, p53DN-hNSCs and p53DN-AKT-hNSCs.

(C) Immunoblots showing WNT5A/CaMKII pathway in BOX5 (100uM) treated p53DN-hNSCs with overexpressed myr-AKT or WNT5A.

(D) Representative FACS showing the percentage of $CD133^{+}/CD144^{+}$ cells in p53DN- hNSCs that overexpress myr-AKT or WNT5A under treatment with WNT5A antagonist BOX5 (50 μM) for 72 hr.

(E) Immunoblots showing WNT5A/CaMKII pathway in $CD133^{+}/CD144^{+}$ cells sorted from p53DN-AKT-hNSCs with BOX5 treatment (100uM).

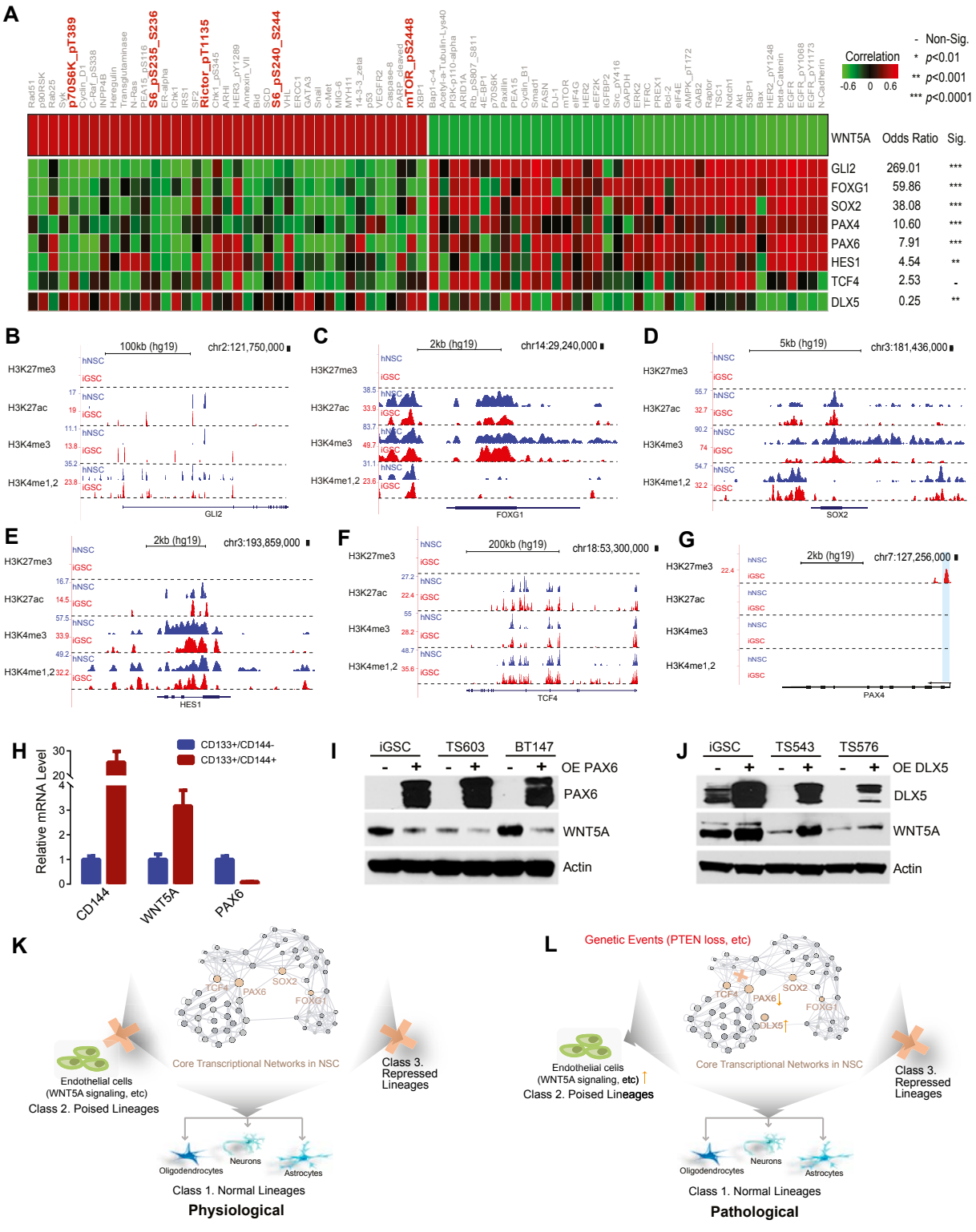

(legend on next page)

Figure S4. Association among mTOR/S6K Pathway, WNT5A, and NSC Master Transcription Factors, Related to Figure 4

(A) Heatmap showing the correlation between WNT5A and NSC master transcription factors (TFs) in the context of mTOR/S6K pathway. TCGA GBMs (IDH wild-type, n = 158) with both proteomic (RPPA) and transcriptomic datasets were used to calculate the correlation between gene expression and protein levels by Spearman rank correlation (red/green color indicating positive/negative correlation). The first row shows expression correlation between the levels of indicated proteins and WNT5A mRNA. The proteins with a Spearman correlation coefficient higher than 0.1 or less than −0.1 are shown. The correlation between TFs and WNT5A was calculated by Fisher exact test; the odds ratios and significances are shown.

(B–G) Chromatin modification changes from pre-malignant state (hNSC) to malignant state (iGSC) for transcription factors, Gli2 (B), FoxG1 (C), SOX2 (D), HES1 (E), TCF4 (F), and PAX4 (G).

(H) qRT-PCR for CD144, WNT5A and PAX6 mRNA levels on the sorted $CD133^{+}/CD144^{-}$ and $CD133^{+}/CD144^{+}$ cells from p53DN-AKT-hNSCs. Error bars represent SD of the mean (n = 3). Immunoblot showing PAX6 (I) and DLX5 (J) overexpression in indicated GSCs. Cartoons showing models of WNT5A transcriptional network involving in plasticity and multiple lineage differentiation of neural stem cell in physiological (K) and pathological (L) situation.

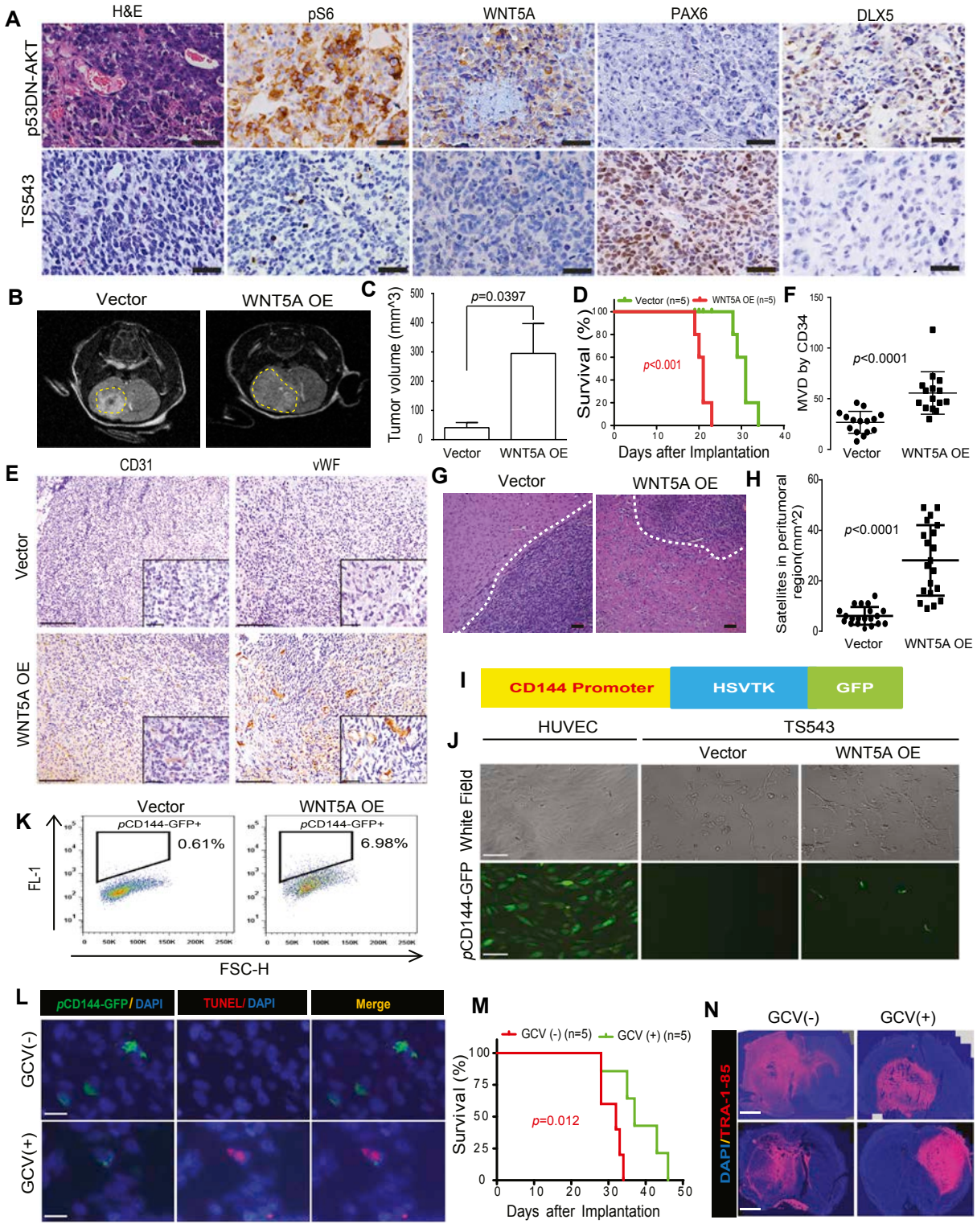

(legend on next page)

Figure S5. Overexpression of WNT5A in Patient-Derived GSCs Increases Vascularization and Invasiveness, Related to Figure 5

(A) Compared with xenograft tumor derived from p53DN-AKT-hNSCs (p53DN-AKT), representative images show that xenograft tumors derived from patient-derived GSC TS543 display lower levels of activation of AKT/mTOR pathway (pS6), lower levels of WNT5A and DLX5, and higher levels of PAX6. Scale bars, 50 μm.

(B) Representative magnetic resonance images from SCID mice after intracranial injection of TS543 overexpressing WNT5A (WNT5A OE) or empty vector as control (Vector). T2 sequences demonstrate infiltrative tumors in mouse brain (yellow line).

(C) Tumor volume was measured by T2 MRI scan (n = 5).

(D) Kaplan–Meier tumor-free survival analysis. TS543 cells overexpressing empty vector (Vector) or WNT5A (WNT5A OE) were implanted into SCID mouse brains. Numbers of animals are indicated; *p* value was calculated by log-rank test.

(E) Representative IHC images of endothelial marker expression (CD31 and vWF) with low (Scale bars, 100 μm) and high (Scale bars, 50 μm) magnification for tumor sections.

(F) Quantitation of MVD evaluated by CD34 staining (n = 3 tumors, 5 fields per tumor).

(G) Representative images of tumor edge between WNT5A OE versus Vector by H&E staining. Scale bars, 100μm.

(H) Quantitation of the number of satellites (> 3 nuclei close together) in peritumoral regions (~0.3 mm^2) by IF staining (n = 4 tumors, 5 fields per tumor).

(I) Schematic illustration of CD144-promoter-driven expression of HSVTK and GFP (*p*CD144-GFP).

(J) Representative images showing GFP expression driven by CD144 promoter only in HUVEC and TS543 overexpressing WNT5A (WNT5A OE) compared with control (Vector). Scale bars, 100μm.

(K) Representative FACS analysis of GFP expression in human sphere line TS543 transduced with lentivirus carrying *p*CD144-GFP.

(L) TUNEL staining of apoptotic cells in GFP positive cells with *p*CD144-GFP in tumors after GCV treatment for one week, Scale bars, 25μm.

(M) Kaplan–Meier tumor-free survival analysis. TS543 cells overexpressing WNT5A were implanted into SCID mouse brain and mice were treated with/out GCV. Numbers of animals are indicated; *P* value was calculated by log-rank test.

(N) Representative images showing tumors in SCID mouse brains with/out GCV treatment. Tumor cells were labeled by TRA-1-85 antibody staining (red). Scale bars, 2000 μm.

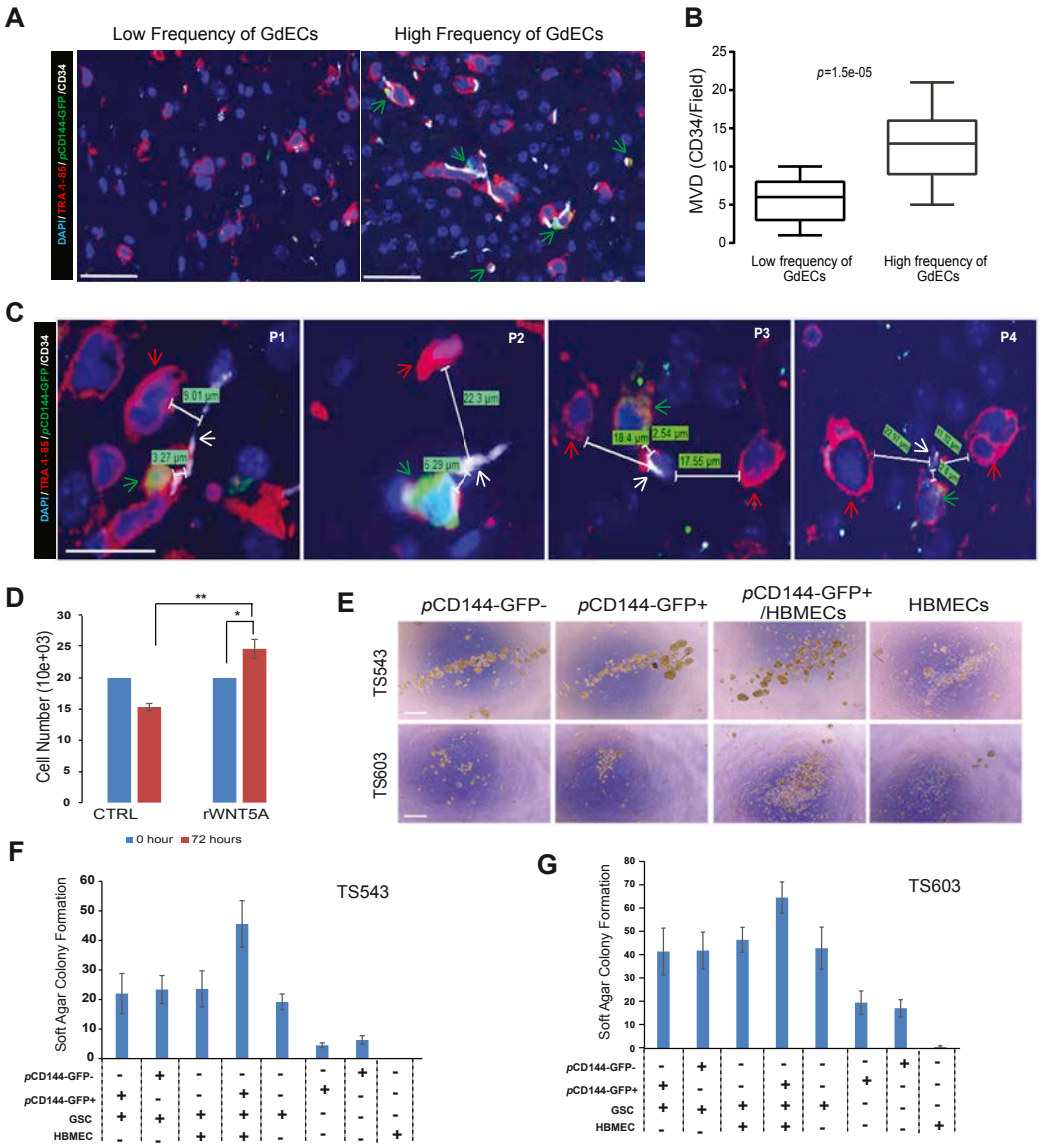

Figure S6. WNT5A-Mediated GdECs Recruit Existing ECs for GSC Growth, Related to Figure 6

(A) Representative images showing the density of existing endothelial cells (TRA-1-85$^-$/CD34$^+$) and GdECs (*p*CD144-GFP$^+$, green arrows) in the peritumoral areas. Scale bars, 50 μm.

(B) Boxplots show the CD34-based MVD analyzed in peritumoral areas with low (less than 5%) and high (more than 5%) frequency of GdECs (n = 3 tumors, 5 fields per tumor).

(C) Representative images show the distance between mouse endothelial cells (TRA-1-85$^-$/CD34$^+$, white arrows) and the nearest GdECs (*p*CD144-GFP$^+$, green arrows)/tumor cells (TRA-1-85$^+$/GFP$^-$, red arrows) in multiple peritumoral areas (P1-P4). Scale bar, 25 μm.

(D) The number of HBMECs was counted after 72 hr treated with/without rWNT5A at 0.5 μg/ml in serum-free EC media. Error bars represent SD of the mean, n = 3; $^*p < 0.05$, $^{**}p < 0.01$.

(E) Representative images showing neurosphere formation of TS543 and TS603 co-cultured with GdECs and/or HBMECs in transwell for 7 days. Scale bars, 200 μm.

Soft agar colony formation assay in 48-well plate showing anchorage-independent growth capability of GSC co-culturing with GdECs and HBMECs in TS543 (F) and TS603 (G) Error bars represent SD of the mean for 5 wells.

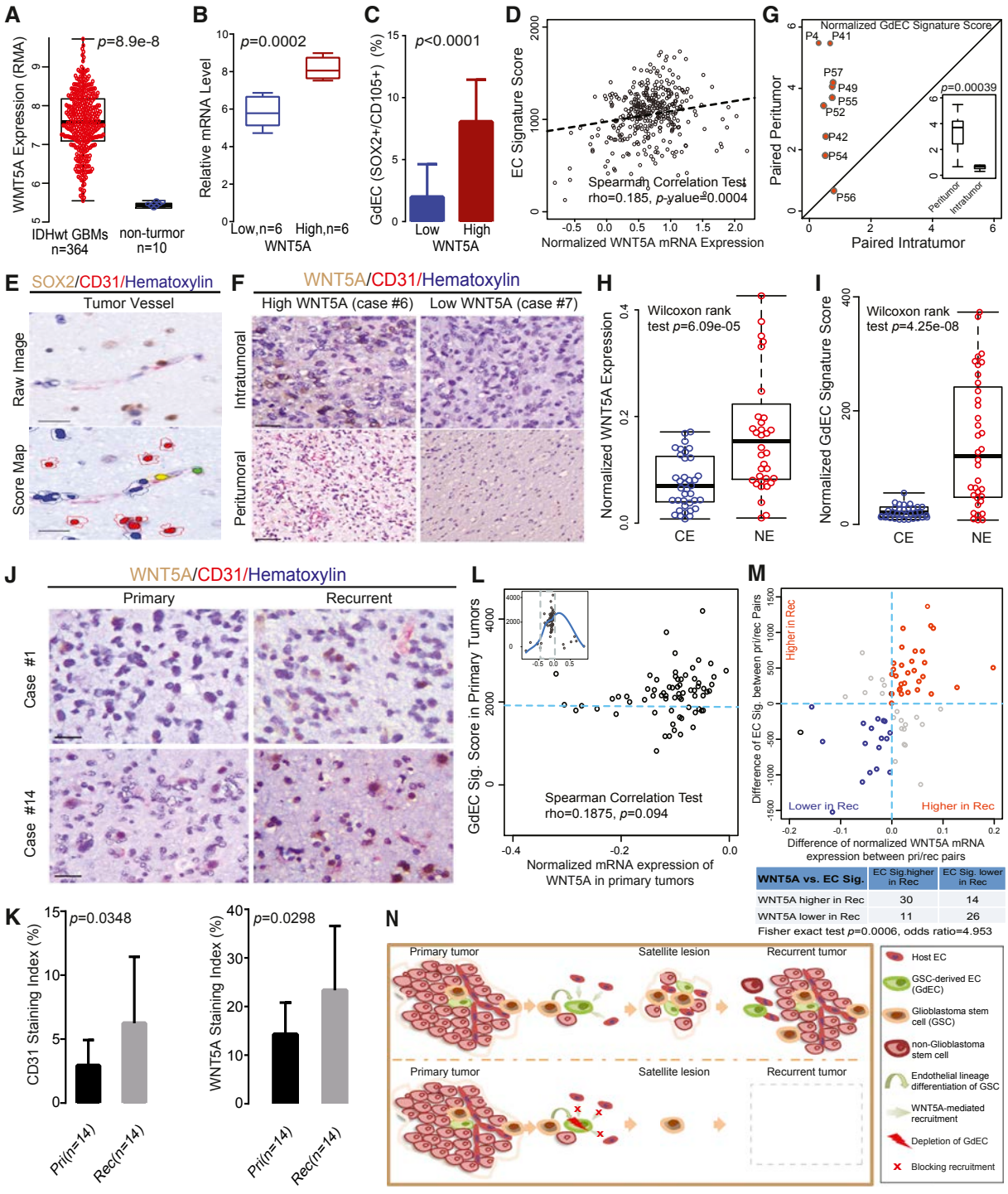

Figure S7. WNT5A and GdECs Are Strongly Correlated with Tumor Recurrence in Human GBMs, Related to Figure 7

(A) WNT5A mRNA expression in TCGA IDHwt GBM tumors compared to non-tumor brain tissues. Gene expression was normalized by RMA and *p* value was calculated by Wilcoxon Rank test.

(B) Two groups, Low WNT5A (n = 6) and High WNT5A (n = 6), show the average of WNT5A mRNA level for 12 fresh GBM specimens (IDHwt) from TCGA.

(legend continued on next page)

(C) The quantitation of GdEC ($CD105^+/SOX2^+$) percentage in 12 tumors from Low and High WNT5A groups. The *p* value was calculated by unpaired Student's t test in two groups.
(D) Correlation between WNT5A mRNA expression and EC signature score (n = 364 IDHwt); mRNA expression was normalized across genes.
(E) Identification of GdECs in tumor vessels by an automated quantitative pathology imaging system. Representative images with IHC double-staining and cell segmentation obtained from Caliper InForm analysis software show tumor vessels with close proximity of GdEC ($SOX2^+/CD31^+$, yellow) and host ECs ($SOX2^-/CD31^+$, green) in GBM patient specimens. $SOX2^+/CD31^-$ cells are marked in red color and $SOX2^-/CD31^-$ cells are marked in blue color. Scale bars, 20 μm.
(F) Representative IHC images show WNT5A and CD31 staining in the primary tumors of two patients with peritumoral satellite lesions. Scale bars, 25 μm (top panel); 50 μm (bottom panel).
(G) Comparison of GdEC signature score between 9 pairs of intratumor and peritumor regions from GBM patients. Each dot represents a pair. Boxplot summarizes the distribution of GdEC signature score in 9 intratumor and peritumor regions, respectively.
(H and I) Boxplots showing WNT5A expression and GdEC signature score in 39 samples from contrast-enhancing (CE) regions and 36 samples from non-enhancing (NE) regions from 27 different glioma patients.
(J) Representative double-stained IHC images show WNT5A and CD31 staining in paired primary and recurrent GBM from 2 patients. Scale bars, 25 μm.
(K) Quantification of WNT5A and CD31 staining index in 14 paired primary and recurrent GBMs. The *p* values were calculated by Wilcoxon signed-rank test.
(L) Correlation between WNT5A expression and GdEC signature scores in primary GBMs. Boxplot inset shows all the 81 pairs, while large boxplot panel shows the majority of samples (n = 69).
(M) Association of differences of WNT5A mRNA expression and EC signature score between 81 matched primary/ recurrent GBMs pairs. Each circle represents a GBM pair. The mRNA expression was normalized across genes.
(N) Cartoon showing the model for GSC-EC differentiation and recruitment contributing to satellite lesions formation and tumor recurrence. It may be possible to block tumor recurrence by targeting this process.